Article

The whisking oscillator circuit

https://doi.org/10.1038/s41586-022-05144-8

Received: 26 May 2021

Accepted: 25 July 2022

Published online: 31 August 2022

Check for updates

Jun Takatoh[1,2,12]✉, Vincent Prevosto[1,2,12], P. M. Thompson[1,3], Jinghao Lu[1,2], Leeyup Chung[4,5,6], Andrew Harrahill[1], Shun Li[2], Shengli Zhao[2], Zhigang He[4,5,6], David Golomb[7,8,9], David Kleinfeld[10,11] & Fan Wang[1,2]✉

Central oscillators are primordial neural circuits that generate and control rhythmic movements[1,2]. Mechanistic understanding of these circuits requires genetic identification of the oscillator neurons and their synaptic connections to enable targeted electrophysiological recording and causal manipulation during behaviours. However, such targeting remains a challenge with mammalian systems. Here we delimit the oscillator circuit that drives rhythmic whisking—a motor action that is central to foraging and active sensing in rodents[3,4]. We found that the whisking oscillator consists of parvalbumin-expressing inhibitory neurons located in the vibrissa intermediate reticular nucleus ($vIRt_{PV}$) in the brainstem. $vIRt_{PV}$ neurons receive descending excitatory inputs and form recurrent inhibitory connections among themselves. Silencing $vIRt_{PV}$ neurons eliminated rhythmic whisking and resulted in sustained vibrissae protraction. In vivo recording of opto-tagged $vIRt_{PV}$ neurons in awake mice showed that these cells spike tonically when animals are at rest, and transition to rhythmic bursting at the onset of whisking, suggesting that rhythm generation is probably the result of network dynamics, as opposed to intrinsic cellular properties. Notably, ablating inhibitory synaptic inputs to $vIRt_{PV}$ neurons quenched their rhythmic bursting, impaired the tonic-to-bursting transition and abolished regular whisking. Thus, the whisking oscillator is an all-inhibitory network and recurrent synaptic inhibition has a key role in its rhythmogenesis.

The vibrissa intermediate reticular nucleus (vIRt)—a caudal ventral medulla region situated medial to the compact part of the nucleus ambiguus—has previously been shown to be the site of the central oscillator for whisking[5]. Using kainic-acid-induced persistent whisking in anaesthetized rats, it was found that the vIRt contains neurons that fire at either the protraction or, predominantly, the retraction phase of whisking[5,6]. Rhythmic whisking is probably driven by an oscillatory signal from inhibitory vIRt neurons that fire during the retraction phase and provide inhibitory inputs onto vibrissa facial motor nucleus (vFMN) neurons, counteracting the tonic excitatory drive[7] (Fig. 1a). These studies led to a model in which tonic excitation of vFMN motoneurons leads to protraction, which is stopped by rhythmic inhibition from vIRt oscillator cells that induces retraction, resulting in the back-and-forth whisking of rodents[4] (Fig. 1a). Furthermore, rhythmic inhibition from vIRt oscillator cells is thought to be reset by inputs from the breathing centre, the pre-Bötzinger complex (preBötC)[8], that drives inhalation[5,7,9].

Oscillator circuits are very difficult to study in mammalian systems. The lack of molecular identification limits the ability to investigate physically distributed circuits at the neuronal level. Targeting brainstem and spinal cord circuits for in vivo recording in awake behaving animals also adds to the challenge. We therefore set out to find putative molecular markers of vIRt whisking oscillator neurons, with an immediate goal of recording and manipulating the identified neurons in awake behaving mice and a subsequent goal of delineating mechanisms of rhythm generation.

Parvalbumin-expressing vIRt premotor neurons

We used a recently developed three-step monosynaptic rabies virus tracing method that enables transsynaptic tracing of premotor neurons in adult mice[10] (Fig. 1b). This method efficiently labelled vibrissa premotor neurons in adult mice and revealed the presence of premotor cells in the vIRt (Fig. 1c). Multiplexed hybridization chain reaction (HCR) RNA fluorescence in situ hybridization (RNA-FISH)[11] analysis revealed that 67.0 ± 1.0% ($n = 4$) of all premotor neurons within the vIRt expressed the inhibitory neuronal marker *Slc32a1* (also known as *vGat*) (Fig. 1c), whereas 28.3 ± 2.0% ($n = 3$) expressed the excitatory neuronal marker *Slc17a6* (also known as *vGlut2*) (Extended Data Fig. 1a,b). Through candidate marker analysis, we found that 69.6 ± 3.4% ($n = 4$) of these *vGat*$^+$ premotor vIRt neurons co-expressed parvalbumin (*Pvalb*, hereafter *PV*) (Fig. 1c and Extended Data Fig. 1b), hereafter denoted $vIRt_{PV}$ neurons. To specifically label and manipulate $vIRt_{PV}$ neurons, we used the split-Cre strategy, taking advantage of the *PV-creN* knock-in mouse line in which the N-terminal half of Cre (*creN*) is expressed from the *PV* genomic locus[12,13]. This involves injecting a retrograde lentivirus (RG-LV) that expresses the C-terminal

[1]Department of Brain and Cognitive Sciences, McGovern Institute for Brain Research, Massachusetts Institute of Technology, Cambridge, MA, USA. [2]Department of Neurobiology, Duke University, Durham, NC, USA. [3]Department of Biomedical Engineering, Duke University, Durham, NC, USA. [4]F.M. Kirby Neurobiology Center, Boston Children's Hospital, Boston, MA, USA. [5]Department of Neurology, Harvard Medical School, Boston, MA, USA. [6]Department of Ophthalmology, Harvard Medical School, Boston, MA, USA. [7]Department of Physiology and Cell Biology, Ben Gurion University, Be'er Sheva, Israel. [8]Department of Physics, Ben Gurion University, Be'er Sheva, Israel. [9]Zlotowski Center for Neuroscience, Ben Gurion University, Be'er Sheva, Israel. [10]Department of Physics, University of California at San Diego, La Jolla, CA, USA. [11]Department of Neurobiology, University of California at San Diego, La Jolla, CA, USA. [12]These authors contributed equally: Jun Takatoh, Vincent Prevosto. ✉e-mail: jtakatoh@mit.edu; fan_wang@mit.edu

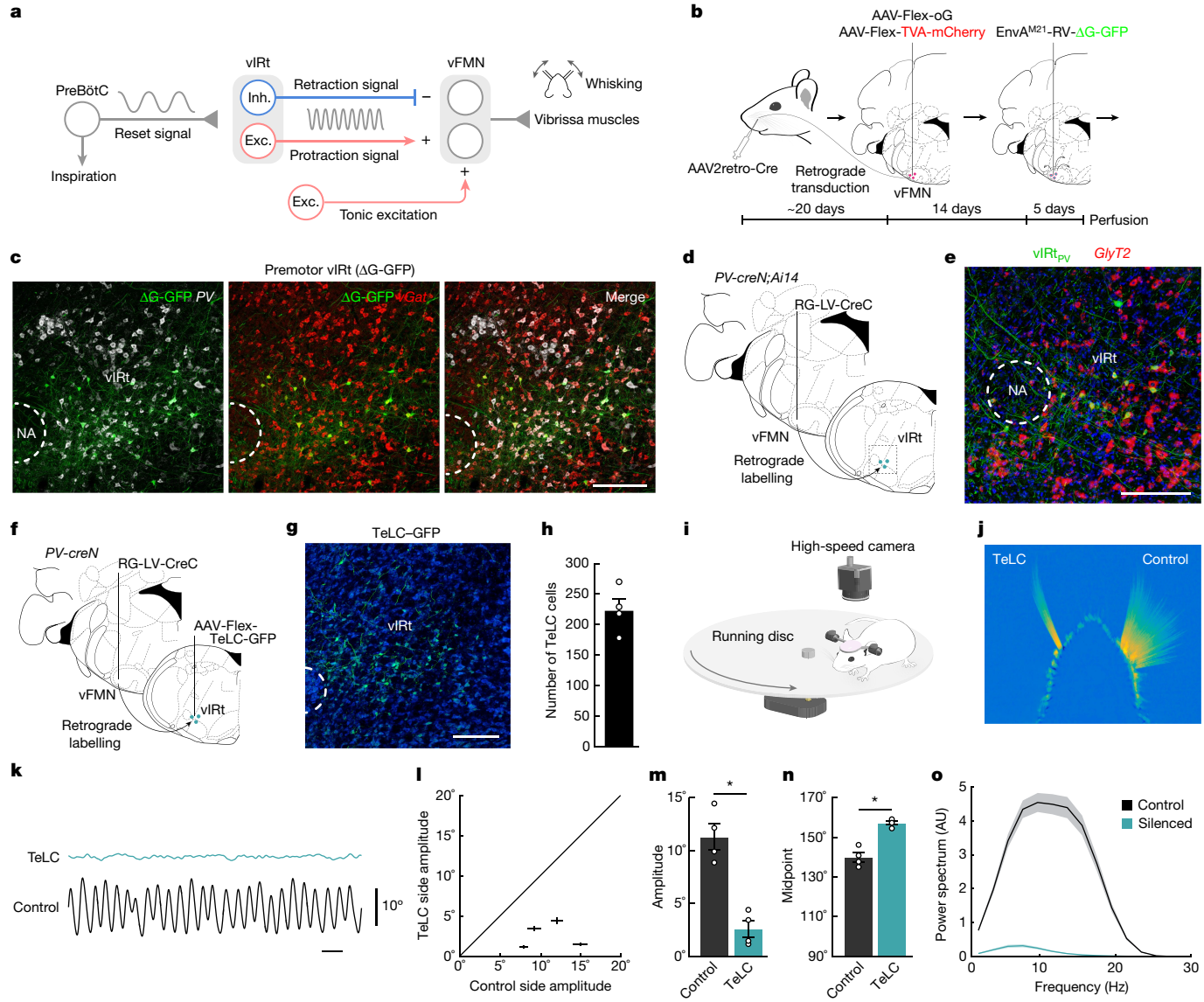

Fig. 1 | Molecular and functional characterization of PV⁺ premotor vIRt neurons. a, Diagram of the proposed whisking generation circuit in the brainstem. Exc., excitatory; Inh., inhibitory. **b**, A three-step monosynaptic rabies virus tracing strategy to label the adult vibrissa premotor circuit. **c**, Representative image of vibrissa premotor neurons in the vIRt. *PV* and *vGat* mRNA were detected using HCR RNA-FISH. NA, nucleus ambiguus. **d**, Viral-genetic split-Cre strategy for labelling PV⁺ premotor vIRt neurons. Retrograde lentivirus carrying CreC (RG-LV-CreC) was injected into the vibrissal part of the facial motor nucleus (vFMN) of the *PV-creN;Ai14* mouse. Functional Cre is reconstituted only in vibrissal premotor neurons expressing PV. **e**, Molecular characterization of $vIRt_{PV}$ neurons. $vIRt_{PV}$ neurons expressing tdTomato (shown in green) overlap with *GlyT2* (red, 87.9 ± 1.4%, $n = 3$ mice). **f**, Strategy for expressing TeLC in $vIRt_{PV}$ neurons using the same split-Cre strategy. **g**, Post hoc histological assessment of TeLC–GFP expression. **h**, Quantification of TeLC–GFP-expressing cells in the vIRt (223.8 ± 18.9). $n = 4$ mice. **i**, The experimental set-up for vibrissa tracking. **j**, A superimposed image of tracked vibrissae (C2; left, TeLC-silenced; right, control). **k**, Representative vibrissa angle traces (green, TeLC-silenced; black, control; the whisking midpoint was subtracted; protraction and inspiration are represented by upward deflections). Scale bar, 100 ms. **l**, Plot of whisking amplitude of the TeLC-silenced and control sides. The dots represent individual mice. **m**, Quantification of whisking amplitude (control side, 11.4 ± 1.2°; TeLC side, 2.6 ± 0.8°). $n = 4$ mice. **n**, Quantification of the whisking midpoint (control side, 140.0 ± 2.4°; TeLC side, 157.3 ± 1.0°). $n = 4$ mice. For **m** and **n**, data are mean ± s.e.m. **o**, Power spectrum analysis of whisking frequency. Data are mean ± s.e.m. (shaded areas). AU, arbitrary units. For **m** and **n**, statistical analysis was performed using Kolmogorov–Smirnov tests; $^*P \leq 0.05$. Brain sections were counterstained with Neurotrace Blue (**c**, **g**) or DAPI (**e**). Scale bars, 200 µm (**c**, **e** and **g**).

half of Cre (RG-LV-CreC) into the lateral part of the facial nucleus (vFMN) in *PV-creN* mice. RG-LV infects neurons from axon terminals[14] and the injection therefore resulted in CreC expression in premotor neurons that project to the vFMN. The full-length Cre can then be fully reconstituted only in PV-positive vibrissa premotor neurons (Fig. 1d). Thus, injection of a viral vector carrying a Cre-dependent construct into the vIRt region results in the expression of the desired genes specifically in premotor $vIRt_{PV}$ neurons, such as a fluorescent reporter protein (Fig. 1d,e). FISH analysis revealed that most $vIRt_{PV}$ neurons expressed the glycine transporter gene *Slc6a5* (also known as *GlyT2*) (Fig. 1e; 87.9 ± 1.4%, $n = 3$), indicating that they are mostly inhibitory cells.

Silencing $vIRt_{PV}$ neurons abolishes whisking

To test whether $vIRt_{PV}$ neurons are part of the whisking oscillator, we used the same viral-genetic split-Cre strategy to express tetanus toxin

light chain (TeLC)[15–17] together with GFP in these neurons (Fig. 1f,g). This resulted in TeLC–GFP being expressed in around 200 $vIRt_{PV}$ neurons (Fig. 1h; 224 ± 19 cells, $n = 4$). Importantly, we observed that TeLC-mediated silencing of $vIRt_{PV}$ neurons almost completely abolished the rhythmic movement of vibrissae on the ipsilateral, silenced side (Fig. 1i–l and Supplementary Video 1). Bilateral tracking of the position of C2 vibrissae revealed that, on the TeLC-silenced side, the vibrissae remained in a protracted position, indicating that vibrissa retraction was abolished (Fig. 1j), consistent with past unilateral chemical ablation of the vIRt area[18]. Quantitatively, silencing $vIRt_{PV}$ neurons resulted in a very low whisking amplitude (Fig. 1m; 11.4 ± 1.2° in the control side versus 2.6 ± 0.8° in the TeLC side; $n = 4$, $P = 0.029$, Kolmogorov–Smirnov test); and a protracted midpoint (Fig. 1n; 140.0 ± 2.4° in the control side versus 157.3 ± 1.0° in the TeLC side; $n = 4$, $P = 0.029$, Kolmogorov–Smirnov test). The power spectrum analysis showed that the residual low-amplitude whisking shifted to lower frequencies (Fig. 1o). The effect of TeLC silencing was permanent.

We further validated these results by acutely silencing $vIRt_{PV}$ neurons with the expression of an anion-conducting channelrhodopsin (GtACR)[19] (Extended Data Fig. 2; $n = 6$). Optogenetic silencing suppressed rhythmic whisking during the light on period and resulted in low-amplitude whisking, although the effect was weaker than that of TeLC silencing, probably due to the inefficiency of short-duration optogenetic silencing (Extended Data Fig. 2f,g). Collectively, these results identify $vIRt_{PV}$ neurons as the essential constituents for mediating rhythmic retraction.

$vIRt_{vGlut2}$ cells are not required for whisking

As a subset of premotor vIRt neurons expressed vGlut2 (Extended Data Fig. 1b), we sought to determine whether they also contribute to rhythmic whisking. We used a viral-genetic intersectional method to specifically label and manipulate $vGlut2^+$ premotor neurons in the vIRt, hereafter referred to as $vIRt_{vGlut2}$ neurons. In brief, in *vGlut2-cre* mice, we injected retrograde lentivirus RG-LV-FlpO into the vFMN to infect vibrissa premotor axon terminals, resulting in co-expression of both Cre and FlpO recombinases in $vGlut2^+$ premotor neurons. Subsequently, we injected Cre- and Flp-co-dependent adeno-associated viruses (AAV) (Con/Fon vectors) into the vIRt to express eYFP or optogenetic silencer halorhodopsin (NpHR3.3) in $vIRt_{vGlut2}$ neurons[20,21] (Extended Data Fig. 1c,e). We found that $vIRt_{vGlut2}$ neurons preferentially projected to the dorsolateral and lateral subnuclei of the facial motor nucleus, where motoneurons innervating the vibrissa retractor muscle nasolabialis/maxillolabialis and extrinsic protractor/nares dilator muscle nasolabialis profundus reside, respectively ($n = 3$; Extended Data Fig. 1d′,d″). Both muscles contract at the onset of inspiration but not during intervening whisks[5]. By contrast, $vIRt_{vGlut2}$ neurons showed less innervation of the ventrolateral subnucleus of the facial motor nucleus, which contains motoneurons that drive vibrissa protraction ($n = 3$; Extended Data Fig. 1d‴). NpHR3.3-mediated optogenetic silencing of $vIRt_{vGlut2}$ neurons during whisking did not alter the amplitude, the midpoint or the whisking frequency as judged from the peak of the power spectrum ($n = 6$; Extended Data Fig. 1h–k). Together, these results suggest that $vIRt_{vGlut2}$ neurons are not involved in whisking rhythm generation. Instead, they may have a role in coordinating vibrissal pad movement with sniffing.

$vIRt_{PV}$ transitions into a rhythmic network

In view of the substantial effect of silencing $vIRt_{PV}$ neurons on rhythmic whisking (Fig. 1j–o), we recorded the in vivo activity of $vIRt_{PV}$ neurons in awake whisking mice to assess whether $vIRt_{PV}$ premotor neurons exhibit rhythmic activity during whisking, a required property of central oscillator cells. We first established a preparation in which a head-fixed mouse ran on a wheel while we performed extracellular multielectrode recordings from the vIRt region, with simultaneous tracking of vibrissa movements. For some recordings, we used our Split-Cre viral-genetic strategy to express channelrhodopsin-2 (ChR2) or red-shifted opsin ChRmine[22] in $vIRt_{PV}$ neurons (Fig. 2a and Extended Data Fig. 3). This enabled us to perform 'opto-tagged' recordings of $vIRt_{PV}$ neurons during natural whisking behaviours (Fig. 2b,c). In vivo identification of $vIRt_{PV}$ neurons was achieved by delivering pulses of 473 nm light over the facial nucleus (or 635 nm light through the ear canal for the ChRmine experiments), while searching for neurons with reliable short-latency, low-jitter, light-induced antidromic spikes (Fig. 2b,e–g). We recorded eight well-isolated and opto-tag-confirmed $vIRt_{PV}$ units from seven mice.

We analysed both opto-tagged ($n = 8$) and untagged ($n = 54$) whisking-related vIRt neurons as one group; untagged neurons include recordings from mice with no or insufficient opsin expression. Cells were classified according to their tuning with respect to the preferred whisking phase (Fig. 2h–j). Among cells with whisking-related responses, a large population ($n = 40$) was found with a rhythmic bursting pattern time-locked to whisking (Fig. 2k,l). Most cells (26 out of 40, 65%) were tuned to the retraction phase with a sharply elevated firing rate that often covered a quadrant of the whisking cycle, starting late in the protraction phase and peaking mid-way through the retraction phase (Fig. 2l (bottom left)). Moreover, these cells typically displayed the highest level of spike-phase spectral coherence early in the retraction phase ($|C| = 0.55 \pm 0.14$, mean ± s.d.; Fig. 2k (black markers) and 2m (retraction units)).

Notably, six out of the eight opto-tagged vIRt neurons were tuned to the whisking phase, and all of these $vIRt_{PV}$ cells belonged to the 'retraction' group (blue or red dots in Fig. 2k; Supplementary Video 2), with high spike/phase coherence ($|C| = 0.71 \pm 0.15$). The results suggest that most of $vIRt_{PV}$ neurons indeed spike rhythmically and are selectively active during the retraction phase, consistent with these cells having a central role in generating rhythmic vibrissa retraction[7]. A smaller group of cells (7 out of 40, 17.5%, of phase tuned cells) responded during the protraction phase ($|C| = 0.60 \pm 0.11$; Fig. 2k (green markers) and 2m (protraction units)) while a minority had responses that occurred at other periods of the whisking cycle (5 out of 40, purple dots, 12.5% mid-protraction, $|C| = 0.45 \pm 0.13$; 2 out of 40, yellow dots, 5% mid-late retraction, $|C| = 0.50 \pm 0.19$; Fig. 2k). An unexpected finding was that two out of the eight opto-tagged $vIRt_{PV}$ neurons and ten untagged neurons displayed slower rhythms, with bursting bouts occurring across multiple whisking cycles (Extended Data Fig. 4a,b). These are potentially linked to other orofacial rhythm generators in the brainstem.

Interestingly, the firing patterns of all rhythmic vIRt cells, that is, both retraction and protraction units and including the six opto-tagged $vIRt_{PV}$ retraction neurons, showed asynchronous tonic firing in non-whisking periods of rest. Rhythmic bursting appeared only at the onset of whisking (Fig. 2m–o). This transition was also confirmed by spectral analysis of firing frequencies, which showed that a power of around 15 to 20 Hz emerged during whisking for units tuned to the whisking phase (Fig. 2o and Extended Data Fig. 4c,e), whereas 'slow' units showed a transition to a slower frequency band, similar to the breathing rhythm (Extended Data Fig. 4d,f). Thus, neurons that spike in rhythmic bursts during whisking are seen to transition from tonic firing during non-whisking rest periods to rhythmic bursting at the onset of whisking (Fig. 2m,n). This result strongly suggests that rhythmic firing is not an intrinsic property of $vIRt_{PV}$ neurons but, rather, a network property that is enabled, perhaps by a top-down whisking command that shifts the operating point of the network[23]. This idea was further supported by in vitro recordings of identified $vIRt_{PV}$ neurons in slices. As $vIRt_{PV}$ cells express PV only in the adult stage, our split-Cre-based strategy could only label these cells in adults. Recording from adult brainstem slices is technically highly challenging; we therefore performed cell-attached recordings from labelled $vIRt_{PV}$ cells in slices ($n = 5$; Extended Data Fig. 5). Bath application of high potassium (9 mM; Methods) to elevate neuronal excitability induced $vIRt_{PV}$

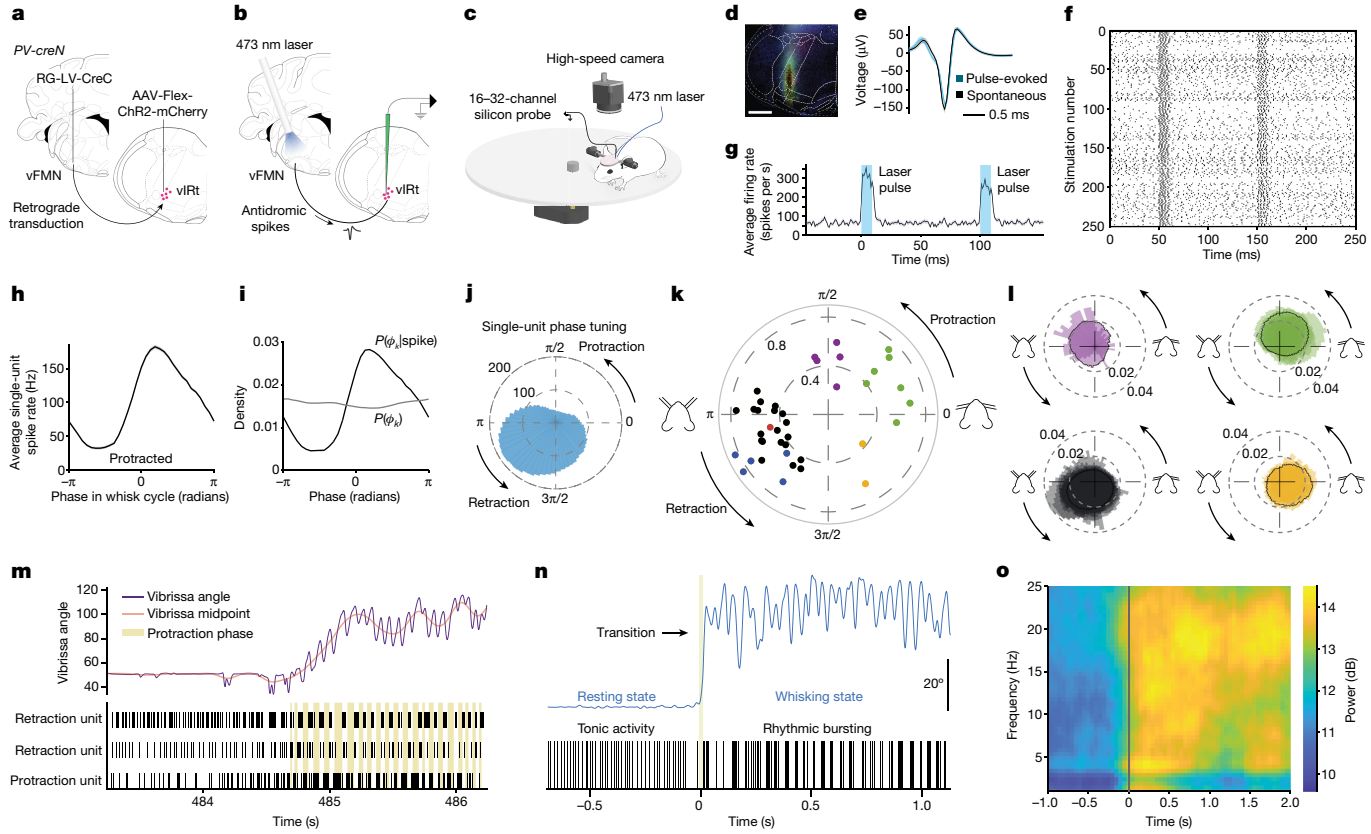

Fig. 2 | Response characteristics of vIRt$_{PV}$ premotor neurons during whisking behaviour. a, The viral-genetic strategy for expressing ChR2 in vIRt$_{PV}$ neurons. **b**, The opto-tagging strategy. **c**, Recording and behavioural set-up. **d**, Histological verification of ChR2 expression and recording location. Scale bar, 500 μm. **e**–**g**, Spike single-unit waveform (**e**), raster plot (**f**) and average laser stimulation response (**g**) of a opto-tagged single unit. **h**–**j**, Whisking phase tuning of a opto-tagged single unit. **h**, The average spike rate across whisking phases. **i**, The probability (*P*) of a particular whisking phase φk occurring for a given spiking event (black) and the probability of each whisking phase (grey). **j**, Phase tuning for the cell from **h**–**i**, in polar coordinates. Magnitude in spikes per second. **k**, The peak magnitude and phase of spike/phase coherence for all tuned cells. Black, blue and red, retraction units; yellow, mid-retraction units; green, protraction units; purple, mid-protraction units. Opto-tagged units are shown in blue or red (ChR2 or ChRmine-expressing cells, respectively). $n = 7$ mice. **l**, The normalized average firing rate of the retraction (bottom left), mid-retraction (bottom right), protraction (top right) and mid-protraction (top left) groups, expressed as a probability value for each phase bin. The colour code is as described in **k**. **m**, The transition from tonic to rhythmic activity pattern. Top, vibrissa angle trace (purple), overlayed with the vibrissa midpoint trace (red). Bottom, raster plot for two retraction and one protraction units. The beige bands mark each protraction phase. **n**, A high-magnification representation of the tonic-to-rhythmic transition that occurs for a retraction-tuned unit going from resting state to whisking movements. **o**, The mean time-frequency spiking spectrum for all retraction units, aligned to the transition from resting to whisking.

neurons to burst, but such bursting was not rhythmic, probably due to the severed-network connectivity in slices that was not sufficient to support rhythm generation.

Presynaptic inputs to the vIRt$_{PV}$ oscillator

We next mapped the presynaptic inputs to vIRt$_{PV}$ neurons as a first step to dissect the circuit-level mechanisms that underlie rhythmic bursting generation during the transition from resting to whisking. We used the same viral-genetic split-Cre strategy to target vIRt$_{PV}$ neurons with AAV helper viruses, followed by injection of pseudotyped monosynaptic rabies virus (EnvA^{M21}-ΔG-GFP)[24–26] (Fig. 3a; $n = 3$), to reveal the major sources of presynaptic inputs to vIRt$_{PV}$ neurons (hereafter, pre-vIRt$_{PV}$ cells; Fig. 3c,d,f and Extended Data Fig. 6). Registration and 3D reconstruction of pre-vIRt$_{PV}$ neurons in Allen Mouse Brain Common Coordinate Framework (hereafter, Allen CCF)[27] revealed consistent labelling patterns across samples (Fig. 3d–f). vIRt$_{PV}$ neurons receive bilateral inputs (with ipsilateral dominance) from the intermediate reticular nucleus (IRt), the parvicellular reticular nucleus (PCRt), the gigantocellular reticular formation, the ventral and dorsal medullary reticular formation (MdV, MdD) and the midbrain reticular nucleus (MRN) located dorsal to the red nucleus (Fig. 3c,f and Extended Data Fig. 6a). Pre-vIRt$_{PV}$ neurons with a predominantly ipsilateral location were observed in the vIRt, preBötC, lateral paragigantocellular nucleus, deep cerebellar nuclei (DCN) and a small number in the spinal trigeminal nuclei (oralis (SpVO), rostral division of the interpolaris (SpIr), and caudal (SpVC) subnuclei) (Fig. 3c,f). vIRt$_{PV}$ neurons also receive inputs from contralateral superior colliculus and the motor cortex (Fig. 3c,f and Extended Data Fig. 6). Interestingly, the MdD, DCN, superior colliculus and MRN were previously identified as premotor areas for vibrissal motoneurons[10,28]. Co-registration of pre-vIRt$_{PV}$ neurons and vibrissa premotor neurons in the Allen CCF further confirmed that those neurons occupy the same spatial locations within the DCN, superior colliculus and MRN, suggesting that these areas may act at both premotor and pre-premotor functional levels to coordinate the activity of motoneurons and the whisking oscillator[10,28,29] (Fig. 3c and Extended Data Fig. 7). Consistent with this idea, axonal collaterals from labelled pre-vIRt$_{PV}$ neurons were also observed to densely innervate the vFMN (Extended Data Fig. 6a). We further characterized neurotransmitter phenotypes of pre-vIRt$_{PV}$ neurons using HCR RNA-FISH (Fig. 3g). We found that the superior colliculus (*vGlut2*/ΔG-GFP, 95.4 ± 3.9%, $n = 4$), MRN (*vGlut2*/ΔG-GFP, 95.4% ± 3.4%, $n = 4$) and DCN (*vGlut2*/ΔG-GFP, 100%, $n = 4$) pre-vIRt$_{PV}$

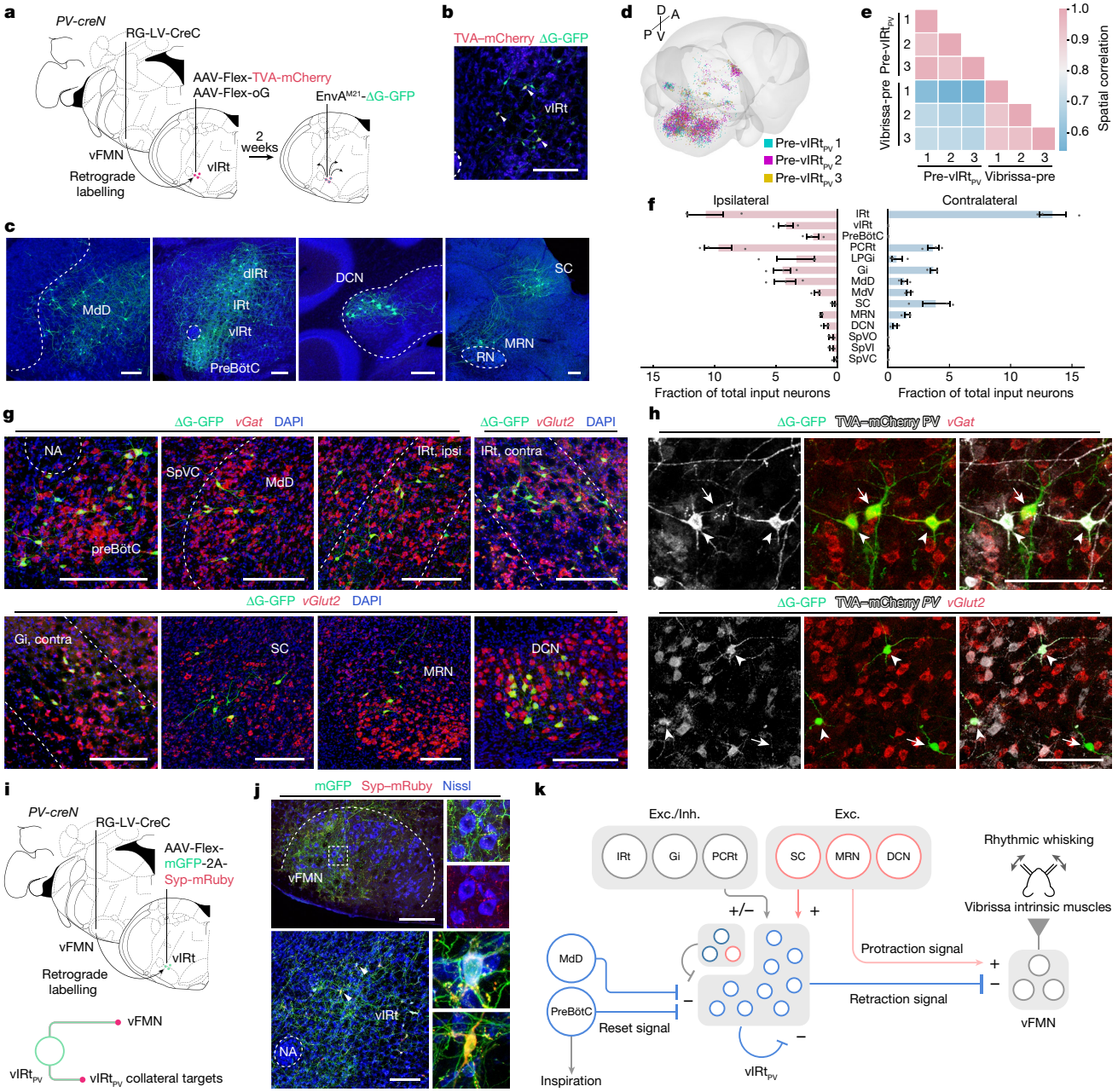

Fig. 3 | Characterizing presynaptic inputs to vIRt$_{PV}$ neurons (pre-vIRt$_{PV}$ cells). a, Schematic of monosynaptic rabies virus tracing in vIRt$_{PV}$ neurons. **b**, TVA–mCherry/GFP double-positive source cells (yellow, arrowheads), and GFP single-positive pre-vIRt$_{PV}$ cells in the vIRt. **c**–**f**, The distribution of pre-vIRt$_{PV}$ neurons. A, anterior; D, dorsal; P, posterior; V, ventral. **c**, Representative images of pre-vIRt$_{PV}$ neurons in the ipsilateral MdD, dIRt, IRt, DCN, preBötC, contralateral superior colliculus and MRN. RN, red nucleus; SC, superior colliculus. **d**, Reconstructed pre-vIRt$_{PV}$ circuits in the Allen CCF (3 mice). **e**, Cross-correlation analysis of pre-vIRt$_{PV}$ cell positions across mice; pre-vIRt$_{PV}$ neurons (3 mice) were compared with vibrissa premotor neurons (vibrissa-pre) (3 mice). **f**, Quantification of the pre-vIRt$_{PV}$ cell number in brain areas. Numbers are normalized to the total number of input neurons. Data are mean ± s.e.m. $n = 3$ mice. Gi, gigantocellular reticular formation; LPGi, lateral paragigantocellular nucleus. **g**, Neurotransmitter characterization of pre-vIRt$_{PV}$ neurons. *vGat* and *vGlut2* mRNA were detected using HCR RNA-FISH. Quantification is shown in Extended Data Fig. 6. Contra, contralateral; ipsi, ipsilateral. **h**, Molecular characterization of pre-vIRt$_{PV}$ neurons within the vIRt. *PV*, *vGat* and *vGlut2* mRNA, and TVA–mCherry protein were detected by HCR RNA-FISH and HCR immunohistochemistry, respectively. Pre-vIRt$_{PV}$ neurons (arrows) are distinguished from source vIRt$_{PV}$ neurons (arrowheads) by their lack of grey-colour-labelled axons/dendrites. **i**, Top, the strategy to identify vIRt$_{PV}$ projections. Bottom, mGFP and Syp–mRuby label the somata/axons and axon terminals, respectively. **j**, Projections of vIRt$_{PV}$ neurons. Top, axonal projections in the vFMN. Bottom, synaptic connections within vIRt$_{PV}$ neurons. Insets: magnified images of the area indicated by the dashed box and the representative vIRt$_{PV}$ neurons receiving mRuby-positive synaptic terminals (arrowheads). Note that strong mGFP-2A-Syp-mRuby expression causes mRuby aggregates in the somata. **k**, Schematic summarizing the presynaptic inputs to the vIRt$_{PV}$. The top left corner of the vIRt indicates PV$^-$vGat$^+$ (deep blue) and vGlut2$^+$ (red) vIRt neurons. The superior colliculus, MRN and DCN provide excitatory inputs to vIRt$_{PV}$ neurons and presumably send simultaneous excitatory protraction signals to the vFMN (translucent red). Scale bars, 200 µm (**b**, **c**, **g** and **j**) and 100 µm (**h**). Sections were counterstained with Neurotrace Blue (**b**, **c** and **j**) or DAPI (**g** and **h**).

neurons were excitatory neurons, whereas preBötC (*vGat*/ΔG-GFP, 86.3 ± 1.8%, $n = 3$) and MdD (*vGat*/ΔG-GFP, 96.6 ± 1.7%, $n = 3$) pre-vIRt$_{PV}$ neurons were mostly inhibitory neurons, and regions of the dorsal IRt (dIRt), gigantocellular reticular formation and parvicellular reticular nucleus provide mixed excitatory/inhibitory inputs to vIRt$_{PV}$ neurons (Fig. 3g and Extended Data Fig. 6).

In addition to the above-mentioned pre-vIRt$_{PV}$ neurons, we noticed GFP single-positive cells in the vIRt region near the source vIRt$_{PV}$ neurons; note that source cells are GFP and TVA–mCherry double-positive (Fig. 3b,c). This suggested that vIRt$_{PV}$ neurons may receive presynaptic inputs from other vIRt$_{PV}$ neurons, that is, vIRt$_{PV}$–vIRt$_{PV}$ synapses as a potential source of recurrent connectivity. To gain further insights into this local circuit, we characterized the molecular identity of pre-vIRt$_{PV}$ neurons within the vIRt (Fig. 3h). We found that the majority of local presynaptic neurons (GFP$^+$TVA–mCherry$^-$ cells in the vIRt) were inhibitory neurons (*PV*$^+$*vGat*$^+$, 49.9 ± 6.4%, $n = 5$; *PV*$^-$*vGat*$^+$, 22.4 ± 4.6%, $n = 5$), whereas 15.5 ± 2.7% ($n = 4$) pre-vIRt$_{PV}$ local inputs were *PV*$^-$*vGlut2*$^+$ excitatory neurons. Note that 67.3 ± 8.3% ($n = 5$) of labelled cells in the vIRt were source cells, suggesting that vIRt$_{PV}$ neurons may form dense recurrent inhibitory network within the vIRt. To further examine this possibility, we sparsely labelled vIRt$_{PV}$ neurons with mGFP–synaptophysin–mRuby[30] (Fig. 3i). In this way, the cell bodies and axons of vIRt$_{PV}$ neurons were labelled by membrane-GFP, whereas the presynaptic boutons on axon terminals from labelled neurons were visualized by mRuby. Dense mGFP-positive vIRt$_{PV}$ axons were observed in the lateral vFMN as expected, further supporting the labelling specificity (Fig. 3j). Interestingly, numerous synaptophysin–mRuby-positive puncta were observed in the vIRt region in both GFP$^+$ (Fig. 3j) and GFP$^-$ cells.

Collectively, these results strongly suggest that vIRt$_{PV}$ neurons form inhibitory synapses onto other vIRt$_{PV}$ neurons, probably resulting in a recurrent inhibitory network (Fig. 3j). We do not know the nature of GFP$^-$ (vGat$^+$) vIRt cells that receive vIRt$_{PV}$ synapses. As we and previous studies in ketamine/xylazine-anaesthetized mice with kainic-acid-induced whisking[5,7] found some vIRt rhythmic neurons firing in the protraction phase, one possibility is that GFP$^-$ vIRt (vGat$^+$) cells are protraction units, and that vIRt$_{PV}$ retraction neurons form reciprocal inhibitory connections with them. In summary, vIRt$_{PV}$ neurons receive descending excitatory presynaptic inputs from the contralateral superior colliculus, MRN, motor cortex and ipsilateral DCN, and inhibitory inputs from the ipsilateral preBötC, MdD and from other vIRt$_{PV}$ and perhaps non-PV vIRt neurons, as well as mixed (excitatory and inhibitory) inputs from IRt and gigantocellular reticular formation (Fig. 3g and Extended Data Figs. 6 and 7).

Role of vIRt$_{PV}$ inhibitory synapses in whisking

Previous studies have established the prominent role of recurrent inhibition in rhythm generation in several systems[1,31–34]. Computational modelling further described a key role of inhibition in vIRt rhythm generation[35]. To test the causal role of inhibition in vIRt$_{PV}$ neuron rhythmogenesis, we used a strategy to specifically ablate the inhibitory post-synapses in vIRt$_{PV}$ neurons. Using the viral-genetic split-Cre strategy, we expressed a Cre-dependent GFE3–eGFP construct in vIRt$_{PV}$ neurons (Fig. 4a). GFE3 is a gephyrin-specific ubiquitin ligase that targets the key inhibitory postsynaptic scaffolding protein gephyrin for degradation, which in turn prevents the clustering of γ-aminobutyric acid type A and glycine receptors[36]. Neurons expressing GFE3 were previously shown to receive significantly diminished phasic synaptic inhibition[36]. This manipulation would, in principle, block all phasic inhibitory inputs to the vIRt$_{PV}$, including those from the preBötC and from other vIRt$_{PV}$ neurons (Fig. 4a). Post hoc histological assessment using anti-gephyrin antibodies in vIRt$_{PV}$-GFE3 mice ascertained the significant reduction of gephyrin signal in GFP-positive cells compared with GFP-negative neighbouring cells (the normalized density of gephyrin puncta in control neighbouring neurons is 0.44 ± 0.01, $n = 76$ cells, $n = 4$ mice; and in GFE3–GFP neurons, 0.14 ± 0.007, $n = 78$ cells, $n = 4$ mice, $P = 0.0286$, Kolmogorov–Smirnov test; Fig. 4b,c).

After at least three weeks of GFE3 expression, we tracked the whisking behaviour of the mice. vIRt$_{PV}$-GFE3 mice were able to initiate whisking, but their vibrissa movement showed several abnormalities (Fig. 4d–i). First, whisking in the air by vIRt$_{PV}$-GFE3 mice was highly irregular compared to the near sinusoidal pattern observed in the control mice. In normal mice, the amplitude of individual whisks does not vary substantially during the whisking epoch (Fig. 4d, bottom trace). By contrast, in vIRt$_{PV}$-GFE3 mice, higher-amplitude whisks were mixed with multiple low-amplitude jitters (Fig. 4d (top trace, arrowheads)). An analysis of whisking regularity with state transition matrix analysis yielded a near elliptical pattern in control mice, indicative of consistent whisking amplitude and frequency from whisk to whisk (Fig. 4e (left)). By contrast, this analysis in vIRt$_{PV}$-GFE3 mice showed a collapsed eclipse, resulting from the poor relationship between current and future vibrissa positions, that is, irregular whisking (Fig. 4e (right)). Moreover, the overall whisking amplitude was significantly smaller in vIRt$_{PV}$-GFE3 mice (control, 34.9 ± 3.0°, $n = 7$; vIRt$_{PV}$-GFE3, 18.7 ± 2.3°, $n = 7$, $P = 0.0047$, Kolmogorov–Smirnov test; Fig. 4f). Taken together, perturbing synaptic inhibition onto vIRt$_{PV}$ neurons markedly impaired the generation of regular patterns of synchronous rhythm.

In contrast to TeLC silencing of vIRt$_{PV}$ neurons, which resulted in increased protraction (Fig. 1n), the whisking midpoint was not affected in vIRt$_{PV}$-GFE3 mice (control, 117.4 ± 3.4°, $n = 7$; vIRt$_{PV}$-GFE3, 104.1 ± 17.8°, $n = 7$, $P = 0.58$, Kolmogorov–Smirnov test; Fig. 4f). One might expect that disinhibition of vIRt$_{PV}$-GFE3 neurons result in a stronger net inhibitory output from these cells, and therefore a larger retraction amplitude; this scenario is valid only if the output of vIRt$_{PV}$-GFE3 neurons were synchronous. The observed unaffected midpoint but significantly smaller amplitude of whisking (Fig. 4f) suggest that vIRt$_{PV}$-GFE3 neurons had greater, but desynchronized inhibitory outputs to vFMN neurons. These findings further support the model that lateral, vIRt$_{PV}$-to-vIRt$_{PV}$ inhibitory synaptic connections have a key role in generating synchronous rhythmic bursting.

A further point is that the frequency of whisking was drastically reduced in vIRt$_{PV}$-GFE3 mice, and the peak frequency was shifted from around 13 Hz (grey line in Fig. 4i) in control mice to around 6–7 Hz in vIRt$_{PV}$-GFE3 mice (Fig. 4i (green line)). The latter value is similar to the frequency of breathing (Fig. 4i). Raster plots of protraction and inspiration onset time analysis showed that protraction onsets of whisks largely coincided with the inspiration onsets (Fig. 4g (red line)) in vIRt$_{PV}$-GFE3 mice, and there was an obvious lack of intervening whisking, that is, whisks between breaths, compared with in control mice. Indeed, a 1:1 breathing versus whisking ratio was dominant in vIRt$_{PV}$-GFE3 mice, whereas a 1:2 ratio was dominant in control mice (Fig. 4h). Quantitatively, this led to a correlation of whisking and breathing for vIRt$_{PV}$-GFE3 mice that is large only in the breathing frequency range (control, 0.27 ± 0.02, $n = 7$; vIRt$_{PV}$-GFE3, 0.43 ± 0.03, $n = 7$, $P = 0.0082$, Kolmogorov–Smirnov test; Fig. 4j,k). These data imply that the whisking rhythm in vIRt$_{PV}$-GFE3 mice was mainly controlled by the slower breathing rhythm, consistent with previous findings that the nasolabialis profundus muscle, which is structurally linked to the mystacial pad, and extrinsic muscles that retract the mystacial pad both receive inputs from breathing oscillators[5,7].

Loss of inhibition abolishes vIRt$_{PV}$ rhythm

Finally, we performed in vivo recordings of opto-tagged vIRt$_{PV}$-GFE3 neurons to determine whether the whisking phenotypes that we observed in vIRt$_{PV}$-GFE3 mice indeed resulted from a loss of rhythmic bursting in these neurons after blocking synaptic inhibition. To achieve this, we needed to co-express ChR2 and GFE3 in vIRt$_{PV}$ cells. We generated an AAV vector containing both ChRmine and GFE3: AAV-hSyn-DIO-ChRmine-T2A-EGFP-GFE3. ChRmine made opto-tagged

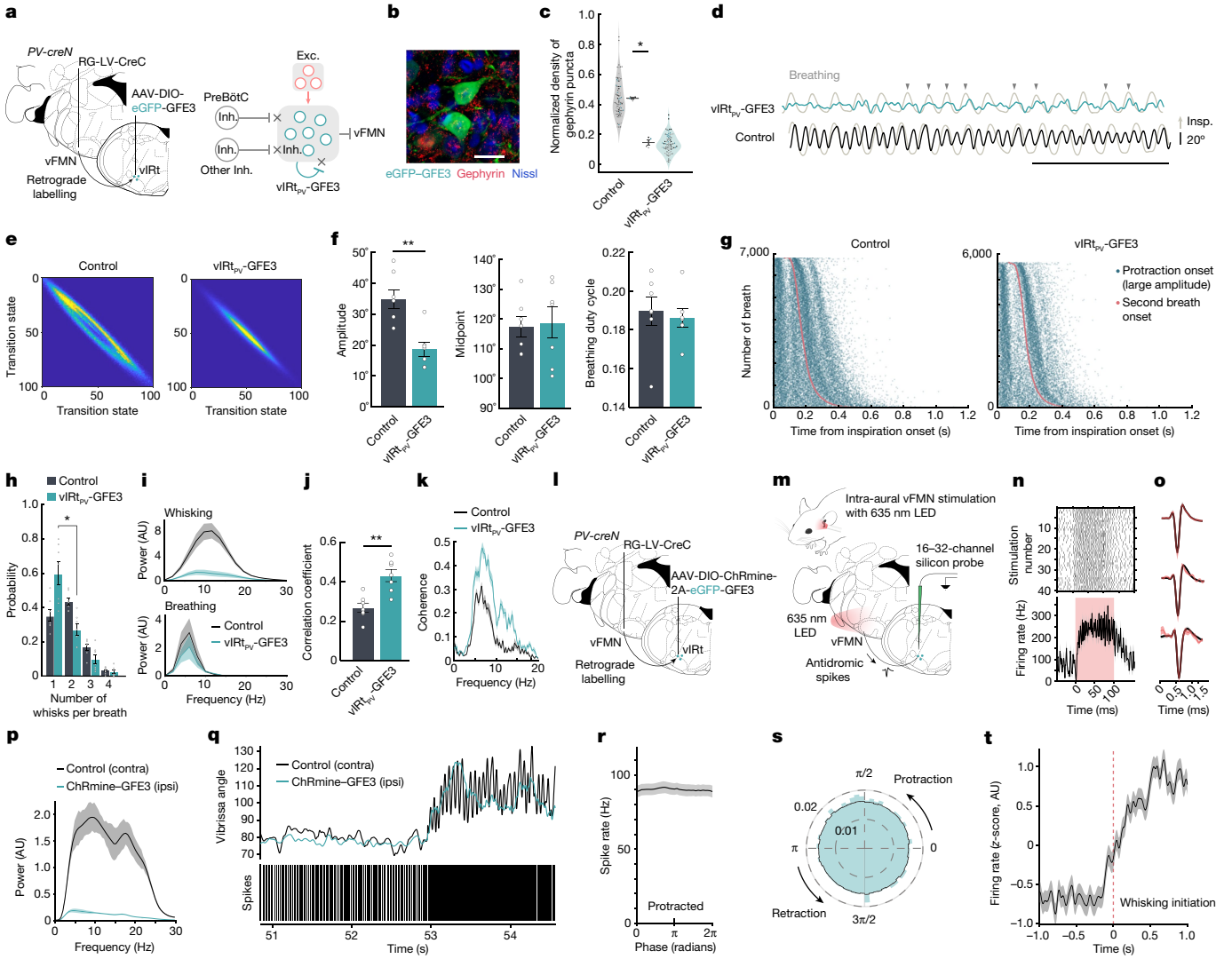

Fig. 4 | Elimination of inhibitory synaptic inputs onto vIRt$_{PV}$ neurons impairs the generation of intervening whisking and abolishes their rhythmic bursting. a, Schematic of the GFE3 (green) post-inhibitory synapse ablation experiment. **b**, Representative image of anti-gephyrin staining in vIRt$_{PV}$-GFE3 neurons. Scale bar, 20 µm. **c**, Quantification of the normalized density of gephyrin puncta (control/neighbouring cells, 0.44 ± 0.006, n = 4 mice, 76 cells; vIRt$_{PV}$-GFE3, 0.15 ± 0.018, n = 4 mice, 78 cells). Data are from individual neurons (dots), colour-coded by mouse. **d**, Vibrissa angle and breathing (light grey) traces from vIRt$_{PV}$-GFE3 (green) and control (black) mice. Protraction and inspiration (Insp.) are represented by upward deflections. Scale bar, 1 s. The downward arrows show correlated breathing/whisking events. **e**, Quantification of whisking regularity using state-transition analysis. **f**, Quantification of whisking amplitude (control, 34.9 ± 3.0°, n = 7 mice; vIRt$_{PV}$-GFE3, 18.7 ± 2.3°, n = 7 mice), midpoint (control, 117.4 ± 3.4°, n = 7 mice; vIRt$_{PV}$-GFE3, 104.1 ± 17. 8°, n = 7 mice) and breathing duty cycle (control, 0.19 ± 0.007, n = 7 mice; vIRt$_{PV}$-GFE3, 0.19 ± 0.004, n = 7 mice). **g**, Raster plots of protraction onset (teal) relative to inspiration onset times (red). Data ordered by breath duration. **h**, Quantification of the number of whisks per one breathing cycle. n = 7 mice. **i**, Power spectrum of whisking and breathing frequency. **j**, Correlation coefficient of breathing and whisking (control, 0.27 ± 0.02, n = 7; vIRt$_{PV}$-GFE3, 0.43 ± 0.03, n = 7). **k**, Coherence between whisking and breathing. **l**, Schematic of the ChRmine-GFE3 opto-tagging experiments. **m**, The opto-tagging strategy. **n**, Raster plot and average stimulation response of a opto-tagged vIRt$_{PV}$-ChRmine-GFE3 single unit. **o**, Average spike waveforms, before (black) and during (red) light stimulation periods for vIRt$_{PV}$-ChRmine-GFE3 single units. n = 3 mice. **p**, Power spectrum of ipsilateral (teal) and contralateral (black) whisking frequency for ChRmine-GFE3 mice. **q**, Unit activity during the transition from resting to whisking state. Top, vibrissa angle traces for ipsilateral (teal) and contralateral (black) C2 vibrissae. Bottom, spike times of an opto-tagged vIRt$_{PV}$-ChRmine-GFE3 neuron. **r**, The average spike rate across whisking phases (derived from contralateral vibrissae) for all opto-tagged vIRt$_{PV}$-ChRmine-GFE3 neurons. **s**, The average spike rate across whisking phases as in **r**, normalized to polar coordinates. **t**, The z-scored average spike rate of vIRt$_{PV}$-ChRmine-GFE3 neurons around the time of whisking initiation. Data are mean ± s.e.m. (**i**, **k**, **n**–**p**, **r** and **t**). Statistical analysis was performed using Kolmogorov–Smirnov tests (**c**, **f**, **i** and **j**) and Wilcoxon signed-rank tests (**g**); $^*P \leq 0.05$, $^{**}P \leq 0.01$.

recordings simpler as we could illuminate through the ear canal to activate ChRmine-expressing vIRt$_{PV}$ axons that project to the vFMN (which reside in close proximity to the inner ear) using a 635 nm LED[22,37] (Fig. 4l–o). Indeed, when we expressed ChRmine alone in vIRt$_{PV}$ neurons (no GFE3 in this case), we recorded a ChRmine-tagged neuron through intraear illumination, and this neuron exhibited rhythmic bursting during the retraction phase, similar to other ChR2-tagged neurons (Fig. 2k and Extended Data Fig. 3). When we expressed both ChRmine and GFE3 in vIRt$_{PV}$ neurons and performed in vivo opto-tagged recording, we found, as expected, that the side expressing ChRmine-GFE3 exhibited irregular small amplitude whisking compared with the control side (Fig. 4p,q and Extended Data Fig. 8). Importantly, vIRt$_{PV}$-ChRmine-GFE3 neurons were no longer capable of firing rhythmic bursts (Fig. 4q–s). Instead, they only tonically increased their firing rates without any

phase tuning when mice transitioned from stationary to active whisking (Fig. 4q–t; the whisking phase was inferred on the basis of the intact contralateral side). These results provide in vivo evidence that recurrent synaptic inhibition is essential for whisking rhythm generation by the $vIRt_{PV}$ oscillator neurons.

Discussion

We identified PV-expressing inhibitory vibrissa premotor neurons in the vIRt, $vIRt_{PV}$, as whisking oscillator neurons and further revealed the putative circuit that underlies synchronous rhythm generation. In vivo recordings in awake mice and in vitro slice recordings showed that $vIRt_{PV}$ oscillator cells are not intrinsic pace-makers. At rest, $vIRt_{PV}$ neurons have non-synchronized tonic activity (a schematic model is shown in Extended Data Fig. 9a) (Fig. 2m,n and Extended Data Fig. 5a). At the initiation of whisking, descending tonic excitatory signals activate the vibrissa protractor motoneurons (vFMN), and at the same time excite $vIRt_{PV}$ neurons, which in turn increase recurrent inhibition within the $vIRt_{PV}$ population. Descending excitation may conceivably also activate other vIRt neurons, including vIRt protraction cells. The combination of increased excitation and recurrent inhibition results in an elevation of inhibitory outputs from $vIRt_{PV}$ and other vIRt inhibitory neurons and, importantly, a transition of $vIRt_{PV}$ cells from tonic firing to a synchronous rhythmic bursting mode. As a consequence, the periodic inhibitory bursts from the $vIRt_{PV}$ suppress the activity of the facial motoneurons. Phasic inhibition from $vIRt_{PV}$ cells results in phasic vibrissa retraction, therefore inducing rhythmic whisking movements[7] (Extended Data Fig. 9b). Previous research showed that, during whisking, breathing can reset whisking[5]. Here we found that inhibitory neurons located in the inspiration oscillator preBötC provide monosynaptic inputs onto $vIRt_{PV}$ neurons. Thus, breathing probably resets whisking through the inhibition of the $vIRt_{PV}$ rhythmic inhibitory signal and the dual inhibition results in the well-documented phenomenon of near-synchronous sniffing and whisking[4,5]. Moreover, breathing oscillators for both inspiration and expiration control nose dilation and mystacial pad retraction motoneurons, which also help to couple the whisking rhythm to breathing[5,7] (Extended Data Fig. 9b).

Our results from two loss-of-function experiments further make the case that $vIRt_{PV}$ neurons are required for rhythmic whisking. When we expressed TeLC in $vIRt_{PV}$ neurons, their rhythmic inhibitory outputs were blocked, resulting in persistent vibrissa protraction caused by the tonic excitation of vFMN motoneurons (Extended Data Fig. 9c). In this case, the recruitment of extrinsic retractor muscles by the breathing oscillators cannot overcome the strong tonic activity of intrinsic protractor muscles, resulting in very limited vibrissa movement (Extended Data Fig. 9c). When we blocked synaptic inhibitory inputs onto $vIRt_{PV}$ neurons through the expression of GFE3, their ability to generate rhythmic bursts in response to descending whisking commands was abolished (Fig. 4). In $vIRt_{PV}$-GFE3 mice, during whisking periods, the increased descending excitation resulted only in an increased tonic firing rate, illustrating the crucial role of external and recurrent inhibitory inputs to the generation of rhythmic bursting. Asynchronous firing of $vIRt_{PV}$-GFE3 neurons lead to the loss of normal whisking rhythm. Stronger and asynchronous inhibitory outputs onto vFMN protractor motoneurons limited whisking to small amplitude and irregular movements, and less protraction than under TeLC synaptic blocking (Extended Data Fig. 9d). Under the GFE3 condition, as the coupling between expiratory oscillators and mystacial pad retraction motoneurons remained intact, the residual whisking followed the breathing rhythm (Extended Data Fig. 9d). In summary, the whisking oscillator consists of inhibitory neurons that individually, at rest, do not have a rhythmogenic property. Rhythm is a network property that emerges with the onset of whisking behaviour and critically depends on recurrent synaptic inhibition.

There are many different schemes that nature uses to generate rhythms for the control of movement[1,2], even as a result of network phenomena[23,38,39]. Notably, oscillators for breathing and locomotion in mammals are known to generate rhythmicity based on excitatory interactions, and the blockade of inhibition does not abolish rhythmicity. Thus, inhibition is not obligatory for rhythmogenesis in the known mammalian oscillators[1,38,40,41]. The crustacean stomatogastric ganglion oscillator contains primarily inhibitory interactions, but the rhythm is produced by pacemakers cells[1]. By contrast, the whisking vIRt oscillator is arguably the first identified network inhibition-based rhythm generator in mammals. This oscillator produces its own rhythm, but can be rapidly entrained by external, phase-setting inputs, in this case from the preBötC. We further suggest that a network oscillator, as opposed to an oscillator formed from intrinsically rhythmic neurons, may enable the oscillator to rapidly change frequencies and amplitudes in response to sensory feedback or a top-down command[42], consistent with the threefold mode of whisking seen in rodents[43]. Thus, the vibrissa oscillator can enable highly adaptive motor behaviours beyond whisking per se.

Online content

Any methods, additional references, Nature Research reporting summaries, source data, extended data, supplementary information, acknowledgements, peer review information; details of author contributions and competing interests; and statements of data and code availability are available at https://doi.org/10.1038/s41586-022-05144-8.

1. Marder, E. & Bucher, D. Central pattern generators and the control of rhythmic movements. *Curr. Biol.* **11**, R986–R996 (2001).
2. Marder, E. & Calabrese, R. L. Principles of rhythmic motor pattern generation. *Physiol. Rev.* **76**, 687–717 (1996).
3. Vincent, S. B. *The Functions of the Vibrissae in the Behavior of the White Rat* (Univ. Chicago, 1912).
4. Welker, W. Analysis of sniffing of the albino rat 1. *Behaviour* **22**, 223–244 (1964).
5. Moore, J. D. et al. Hierarchy of orofacial rhythms revealed through whisking and breathing. *Nature* **497**, 205–210 (2013).
6. Moore, J. D., Deschenes, M., Kurnikova, A. & Kleinfeld, D. Activation and measurement of free whisking in the lightly anesthetized rodent. *Nat. Protoc.* **9**, 1792–1802 (2014).
7. Deschenes, M. et al. Inhibition, not excitation, drives rhythmic whisking. *Neuron* **90**, 374–387 (2016).
8. Smith, J. C., Ellenberger, H. H., Ballanyi, K., Richter, D. W. & Feldman, J. L. Pre-Botzinger complex: a brainstem region that may generate respiratory rhythm in mammals. *Science* **254**, 726–729 (1991).
9. Kleinfeld, D., Deschenes, M., Wang, F. & Moore, J. D. More than a rhythm of life: breathing as a binder of orofacial sensation. *Nat. Neurosci.* **17**, 647–651 (2014).
10. Takatoh, J. et al. Constructing an adult orofacial premotor atlas in Allen mouse CCF. *eLife* **10**, e67291 (2021).
11. Choi, H. M. T. et al. Third-generation in situ hybridization chain reaction: multiplexed, quantitative, sensitive, versatile, robust. *Development* **145**, dev165753 (2018).
12. Bellavance, M. A. et al. Parallel inhibitory and excitatory trigemino-facial feedback circuitry for reflexive vibrissa movement. *Neuron* **95**, 673–682 (2017).
13. Wang, P. et al. Intersectional Cre driver lines generated using split-intein mediated split-Cre reconstitution. *Sci. Rep.* **2**, 497 (2012).
14. Kato, S. et al. A lentiviral strategy for highly efficient retrograde gene transfer by pseudotyping with fusion envelope glycoprotein. *Hum. Gene Ther.* **22**, 197–206 (2011).
15. Link, E. et al. Tetanus toxin action: inhibition of neurotransmitter release linked to synaptobrevin proteolysis. *Biochem. Biophys. Res. Commun.* **189**, 1017–1023 (1992).
16. Schiavo, G. et al. Tetanus and botulinum-B neurotoxins block neurotransmitter release by proteolytic cleavage of synaptobrevin. *Nature* **359**, 832–835 (1992).
17. Zhang, Y. et al. Identifying local and descending inputs for primary sensory neurons. *J. Clin. Invest.* **125**, 3782–3794 (2015).
18. Kleinfeld, D., Moore, J. D., Wang, F. & Deschenes, M. The brainstem oscillator for whisking and the case for breathing as the master clock for orofacial motor actions. *Cold Spring Harb. Symp. Quant. Biol.* **79**, 29–39 (2014).
19. Govorunova, E. G., Sineshchekov, O. A., Janz, R., Liu, X. & Spudich, J. L. Natural light-gated anion channels: a family of microbial rhodopsins for advanced optogenetics. *Science* **349**, 647–650 (2015).
20. Fenno, L. E. et al. Targeting cells with single vectors using multiple-feature Boolean logic. *Nat. Methods* **11**, 763–772 (2014).
21. Fenno, L. E. et al. Comprehensive dual- and triple-feature intersectional single-vector delivery of diverse functional payloads to cells of behaving mammals. *Neuron* **107**, 836–853 (2020).
22. Marshel, J. H. et al. Cortical layer-specific critical dynamics triggering perception. *Science* **365**, eaaw5202 (2019).

23. Kleinfeld, D. & Sompolinsky, H. Associative neural network model for the generation of temporal patterns. Theory and application to central pattern generators. *Biophys. J.* **54**, 1039–1051 (1988).
24. Kim, E. J., Jacobs, M. W., Ito-Cole, T. & Callaway, E. M. Improved monosynaptic neural circuit tracing using engineered rabies virus glycoproteins. *Cell Rep.* **15**, 692–699 (2016).
25. Miyamichi, K. et al. Dissecting local circuits: parvalbumin interneurons underlie broad feedback control of olfactory bulb output. *Neuron* **80**, 1232–1245 (2013).
26. Wickersham, I. R. et al. Monosynaptic restriction of transsynaptic tracing from single, genetically targeted neurons. *Neuron* **53**, 639–647 (2007).
27. Wang, Q. et al. The Allen Mouse Brain Common Coordinate Framework: a 3D reference atlas. *Cell* **181**, 936–953 (2020).
28. Takatoh, J. et al. New modules are added to vibrissal premotor circuitry with the emergence of exploratory whisking. *Neuron* **77**, 346–360 (2013).
29. Sreenivasan, V., Karmakar, K., Rijli, F. M. & Petersen, C. C. Parallel pathways from motor and somatosensory cortex for controlling whisker movements in mice. *Eur. J. Neurosci.* **41**, 354–367 (2015).
30. Beier, K. T. et al. Circuit architecture of VTA dopamine neurons revealed by systematic input-output mapping. *Cell* **162**, 622–634 (2015).
31. Fortin, G., Jungbluth, S., Lumsden, A. & Champagnat, J. Segmental specification of GABAergic inhibition during development of hindbrain neural networks. *Nat. Neurosci.* **2**, 873–877 (1999).
32. Friesen, W. O., Poon, M. & Stent, G. S. An oscillatory neuronal circuit generating a locomotory rhythm. *Proc. Natl Acad. Sci. USA* **73**, 3734–3738 (1976).
33. Grillner, S. Biological pattern generation: the cellular and computational logic of networks in motion. *Neuron* **52**, 751–766 (2006).
34. Marder, E. & Bucher, D. Understanding circuit dynamics using the stomatogastric nervous system of lobsters and crabs. *Annu. Rev. Physiol.* **69**, 291–316 (2007).
35. Golomb, D. et al. Theory of hierarchically-organized neuronal oscillator dynamics that mediate rodent rhythmic whisking. *Neuron* (in the press).
36. Gross, G. G. et al. An E3-ligase-based method for ablating inhibitory synapses. *Nat. Methods* **13**, 673–678 (2016).
37. Lin, J. Y., Knutsen, P. M., Muller, A., Kleinfeld, D. & Tsien, R. Y. ReaChR: a red-shifted variant of channelrhodopsin enables deep transcranial optogenetic excitation. *Nat. Neurosci.* **16**, 1499–1508 (2013).
38. Kiehn, O. Decoding the organization of spinal circuits that control locomotion. *Nat. Rev. Neurosci.* **17**, 224–238 (2016).
39. Song, J. et al. Multiple rhythm-generating circuits act in tandem with pacemaker properties to control the start and speed of locomotion. *Neuron* **105**, 1048–1061 (2020).
40. Janczewski, W. A., Tashima, A., Hsu, P., Cui, Y. & Feldman, J. L. Role of inhibition in respiratory pattern generation. *J. Neurosci.* **33**, 5454–5465 (2013).
41. Del Negro, C. A., Funk, G. D. & Feldman, J. L. Breathing matters. *Nat. Rev. Neurosci.* **19**, 351–367 (2018).
42. Ausborn, J., Snyder, A. C., Shevtsova, N. A., Rybak, I. A. & Rubin, J. E. State-dependent rhythmogenesis and frequency control in a half-center locomotor CPG. *J. Neurophysiol.* **119**, 96–117 (2018).
43. Berg, R. W. & Kleinfeld, D. Rhythmic whisking by rat: retraction as well as protraction of the vibrissae is under active muscular control. *J. Neurophysiol.* **89**, 104–117 (2003).
44. Tervo, D. G. et al. A designer AAV variant permits efficient retrograde access to projection neurons. *Neuron* **92**, 372–382 (2016).

Publisher's note Springer Nature remains neutral with regard to jurisdictional claims in published maps and institutional affiliations.

Springer Nature or its licensor holds exclusive rights to this article under a publishing agreement with the author(s) or other rightsholder(s); author self-archiving of the accepted manuscript version of this article is solely governed by the terms of such publishing agreement and applicable law.

© The Author(s), under exclusive licence to Springer Nature Limited 2022

Methods

Animals

All animal handling and experiment procedures were approved by The Duke University Institutional Animal Care and Use Committee and MIT Committee for Animal Care. Male and female C57B/L6, Gt(Rosa)26Sortm14(CAG-tdTomato)Hze/J (Ai14, JAX 007914, Jackson Laboratory), parvalbumin-CreN knock-in (*PV-creN*)[12] and *vGlut2-cre* knock-in (JAX 028863) were used in this study.

DNA constructs

pAAV-EF1a-DIO-GtACR2-eYFP and pAAV-hSyn-DIO-ChRmine-T2A-eGFP-GFE3 were constructed by standard molecular cloning procedures using enzymes from New England Biolabs. To generate pAAV-EF1a-DIO-GtACR2-EYFP, NheI and AscI sites were added to the 5′ and 3′ ends of the GtACR2-eYFP fragment, respectively, by PCR amplification from pFUGW-hGtACR2-EYFP[19] (Addgene, 67877). This fragment was inserted into the AscI-NheI site of pAAV-Ef1a-DIO-EYFP (Addgene, 27056).

To generate pAAV-hSyn-DIO-ChRmine-T2A-EGFP-GFE3, the custom DNA fragment containing a BamHI-double LoxP-flanked inverted ChRmine-T2A-EGFP-GFE3-NcoI was synthesized by Epoch Life Science. This BamHI–NcoI fragment was inserted into BamHI–NcoI site of pAAV-hSyn-DIO-EGFP (Addgene, 50457).

Viruses

The AAVs used in this study included AAV2retro-CAG-Cre[44] (Boston Children's Hospital Viral Core), AAV2/8-CAG-Flex-TVA-mCherry[25] (Addgene, 48332), AAV2/8-CAG-Flex-oG[24] (Addgene, 74292, Duke Viral Vector Core), AAV2/8-hSyn-FLEX-TeLC-P2A-EYFP-WPRE[17] (Addgene, 135391), AAV2/8-Ef1a-DIO-hChR2(E123A)-mCherry[45] (Addgene, 35508), AAV2/8-EF1a-DIO-GtACR2-EYFP[19], AAV2/1-hSyn-FLEx-mGFP-2A-Synaptophysin-mRuby[30] (Addgene, 71760), AAV2/8-Ef1a-DIO_EGFP-GFE3[36] (Addgene, 79871), AAV2/8-CAG-FLEX-EGFP-WPRE (Addgene, 51502), AAV2/8-hSyn-DIO-ChRmine-T2A-EGFP-GFE3 (this paper), AAV2/8-hSyn-Con/Fon-EYFP[20] (Addgene, 55650) and AAV2/8-nEF-Con/Fon-NpHR3.3-EYFP[21] (Addgene, 137152). RG-LV-CreC[46], RG-LV-FlpO[47] and EnvA(M21)-RV-ΔG-GFP (also called CANE-ΔG-RV) were produced as previously described[48].

Surgery

Monosynaptic rabies virus tracing in vFMN premotor neurons of adult mice. A three-step monosynaptic rabies virus tracing was performed as described previously[10]. In brief, postnatal day 17 C57B/L6 mice were anaesthetized with a mixture of ketamine (100 mg kg^{-1}) and xylazine (10 mg kg^{-1}). AAV2retro-Cre was injected into two sites in the mystacial pad (between the B1–B2 and C1–C2 vibrissae, 500 nl each) using a volumetric injection system (based on a single-axis oil hydraulic micromanipulator; MO-10, Narishige)[49] equipped with a bevelled glass micropipette (Drummond, 5-000-2005). Twenty days or longer after the first injection, the mice were anaesthetized with isoflurane (1–2%), placed in the stereotaxic instrument (Model 963, David Kopf Instruments) and stereotaxically injected with 120 nl of a 1:1 mixture of AAV2/8-CAG-Flex-TVA-mCherry and AAV2/8-CAG-Flex-oG into the lateral part of VII where vibrissa motor neurons reside (vFMN, 5.8 mm posterior, 1.38 mm lateral to the bregma, and 5.2 mm below the brain surface) at a rate of 30 nl min^{-1} using a bevelled glass micropipette equipped with a microsyringe pump (UMP3, WPI) controlled by the Micro4 controller (WPI). Then, 14 days later, 250 nl of EnvA(M21)-RV-ΔG-GFP (diluted at 1:10 in PBS) was injected into the same injection site. Five days later, the mice were perfused for histological analysis.

Labelling and manipulation of vIRt$_{PV}$ neurons. We initially visualized the whole population of PV-positive vFMN premotor neurons (Fig. 1d,e) by stereotaxically injecting RG-LV-CreC into vFMN (1,200 nl, 50 nl min^{-1}) of *PV-creN;Ai14* mice. Three weeks later, the mice were perfused for histological analysis of tdTomato-positive cells throughout the brainstem.

To specifically express a desired gene in vIRt$_{PV}$ neurons in a Cre-dependent manner (Figs. 1–4), *PV-creN* mice were anaesthetized, and RG-LV-CreC was stereotaxically injected into the vFMN (1,200 nl, 50 nl min^{-1}). Cre-dependent AAV (AAV2/8-hSyn-FLEX-TeLC-P2A-eYFP-WPRE (250 nl), AAV2/8-Ef1a-DIO-hChR2(E123A)-mCherry (200 nl), AAV2/8-EF1a-DIO-GtACR2-eYFP (300 nl), AAV2/1-hSyn-FLEx-mGFP-2A-synaptophysin-mRuby (200 nl), AAV2/8-Ef1a-DIO_eGFP-GFE3 (200 nl), AAV2/8-hSyn-DIO-ChRmine-T2A-eGFP-GFE3 (300 nl) or AAV2/8-CAG-FLEX-eGFP-WPRE (300 nl)) were delivered into vIRt (6.6 mm posterior, 0.9 mm lateral to the bregma, 4.9 mm below the brain surface) at a rate of 30 nl min^{-1}.

Labelling and manipulation of vIRt$_{vGlut2}$ neurons. *vGlut2-cre* mice were anaesthetized, and RG-LV-FlpO was stereotaxically injected into the vFMN (800 nl, 50 nl min^{-1}). AAV2/8-hSyn-Con/Fon-eYFP or AAV2/8-nEF-Con/Fon-NpHR3.3-eYFP were delivered into the vIRt (250 nl, 30 nl min^{-1}).

Monosynaptic rabies virus tracing from in vIRt$_{PV}$ neurons. vIRt$_{PV}$ neurons were transduced with 120 nl of a 1:1 mixture of AAV2/8-CAG-Flex-TVA-mCherry and AAV2/8-CAG-Flex-oG using the procedure described above. Then, 14 days later, 250 nl of EnvA(M21)-RV-ΔG-GFP (diluted at 1:10 in PBS) was injected into the vIRt. Then, 5 days later, the mice were perfused for histological analysis.

For the molecular characterization of pre-vIRt$_{PV}$ neurons within the vIRt, a different injection procedure was used to preserve mRNA expression in the vIRt. In this procedure, vIRt$_{PV}$ neurons were transduced with 120 nl of a 1:2 mixture of AAV2/8-CAG-Flex-TVA-mCherry (pre-diluted at 1:5 in PBS) and AAV2/8-CAG-Flex-oG. Then, 10 days later, 250 nl of EnvA(M21)-RV-ΔG-GFP (diluted at 1:10 in PBS) was injected in vIRt. Next, 4 days later, the mice were perfused for HCR RNA-FISH analysis.

Optic fibre and head-post implantation

For the optogenetic silencing of vIRt$_{PV}$ and vIRtv$_{Glut2}$ experiments, an optic fibre (200 µm) was implanted above the vIRt (6.6 mm posterior, 0.9 mm lateral to the bregma, 4.1 mm below the brain surface) after injecting AAV2/8-EF1a-DIO-GtACR2-eYFP or AAV2/8-nEF-Con/Fon-NpHR3.3-eYFP, and affixed to the skull with cyanoacrylate (Super Glue, Loctite) and C&B Metabond (Parkell). For behaviour experiments and electrophysiological recordings, a custom-made metal head-post was attached to the skull with cyanoacrylate and C&B Metabond for head-fixation. For opto-tagging experiments using ChR2, an optic fibre was implanted above the vFMN after ChR2 expression in vIRt$_{PV}$ neurons using the viral strategy described above (5.8 mm posterior, 2.75 mm lateral to the bregma at a 20° angle, 4.5 mm below the brain surface).

Behaviour

Mice were head-fixed using plate clamps (Thorlabs) positioned over a running disk made of a transparent plexiglass disk overlaid with a translucent silicone sheet. The disk was fixed to an optical shaft encoder (US Digital, H5-100-NE-S) to measure the rotation of the disk. Before the behaviour experiments, the mice were habituated to the head-fixation and the running disk. One day before the behavioural experiments, the mice were lightly anaesthetized with isoflurane and all vibrissae except for the C row were trimmed. Vibrissae were illuminated by an infrared LED placed below the running disk and vibrissa movement was recorded using a high-speed camera (Basler) at 500 fps. For the GFE3 experiment, breathing was monitored using an air flow sensor (Honeywell, AWM3303V) placed in front of the nose.

Optogenetic silencing experiment

Mice had to run for 1 s to trigger laser onset and then had to continue running for at least 1 s after to be counted as a trial. Continuous 470 nm

(GtACR2) or 561 nm (NpHR3.3) laser stimulation (Opto Engine, 7–10 mW) was delivered through the implanted optic fibre, lasting until the end of the run. The optic fibre implantation sites were assessed by post hoc histological analysis.

In vivo electrophysiology and opto-tagging experiment

Before recordings, a small craniotomy (0.7 mm × 1 mm) was made over the vIRt coordinates (6.6 mm posterior, 0.9 mm lateral to the bregma). The dura was left intact. During acute recordings, the craniotomy was sealed with artificial dura (Dura-gel, Cambridge Neurotech). Between experiments, a silicone elastomer (Kwik-Cast, WPI) was applied to cover and protect the craniotomy. Finally, a small custom-designed 3D-printed cap was affixed to the head-post to prevent interference with the fibre optic and the craniotomy area.

In a typical recording session, the mouse was placed onto the running wheel, head-fixed and the head-post cap was removed. The craniotomy was exposed and covered with sterile saline. For ChR2 opto-tagging experiments, a 473 nm laser (Cobolt) was connected to the ferrule. For ChRmine opto-tagging experiments, a 635 nm LED (LED635L, Thorlabs) was placed against the ear ipsilateral to the injected side. A 16- or 32-channel silicon probe (Cambridge Neurotech) was then lowered with a micromanipulator (Sutter Instruments) to about 4.7 mm to the IRt region dorsal and medial to the preBötC. Recordings were made at multiple steps going further down, while monitoring orofacial activity and responses to trains of laser stimulation. Signals from the silicon probe were filtered (250 Hz to 6 kHz for spikes, 0.3 Hz to 250 Hz for local field potentials) and recorded at 30 kHz on the Cereplex Direct (Blackrock Microsystems) system. For each recording, video acquisition was piloted and monitored using the open source software Bonsai (https://bonsai-rx.org/)[50]. Within the Bonsai workflow, video frames were triggered through a Teensy 3.2 (PJRC) board and video streams were encoded with FFmpeg (https://ffmpeg.org/). Laser pulse trains were programmed and triggered with a transistor–transistor logic (TTL) pulse generator (OTPG-4, Doric Lenses) controlled by Doric Neuroscience Studio. All TTLs (from the camera, the pulse generator and a master Arduino controlled through Bonsai) were acquired on the Cereplex Direct's digital inputs at 30 kHz. Signals from the rotary encoder and the air flow sensor were recorded on the Cereplex Direct's analogue inputs at 1 kHz and 10 kHz, respectively. At the end of the recording sessions, the Dura-gel was covered with Kwik-Cast and the protective cap was put back into place.

Slice recordings

For slice recording, $vIRt_{PV}$ neurons were labelled in *PV-creN;Ai14* mice or *PV-creN* mice with AAV2/8-CAG-FLEX-eGFP as described above. Injection and recording were performed at postnatal day 21 (P21)–P28 and P49–P56, respectively.

After isofluorane anaesthesia and transcardial perfusion with *N*-methyl-D-glucamine (NMDG) slicing solution, the brains were quickly extracted. Coronal brain slices (250 µm) were cut using a vibratome (Leica VT1200) in ice-cold NMDG slicing solution, kept in NMDG slicing solution (at 34 °C for 12 min), then moved to artificial cerebrospinal fluid (ACSF) solution (at 34 °C for 30 min). Then slices were kept in room temperature before the transfer to the recording chamber maintained at 30 °C in ACSF. NMDG slicing solution consisted of NMDG 92 mM, HEPES 20 mM, $NaHCO_3$ 30 mM, KCl 2.5 mM, NaH_2PO_4 1.25 mM, thiourea 2 mM, Na-ascorbate 5 mM, Na-pyruvate 3 mM, glucose 25 mM, $CaCl_2$ 0.5 mM, $MgSO_4$ 10 mM. ACSF consisted of NaCl 125 mM, KCl 2.5 mM, NaH_2PO_4 1.25 mM, glucose 11 mM, $NaHCO_3$ 26 mM, $MgCl_2$ 1.3 mM, $CaCl_2$ 2 mM. Cell-attached recordings were performed in a loose-seal (20–60 MΩ) configuration, using a glass pipette (3–7 MΩ) in voltage-clamp mode at a holding potential of 0 mV. The pipette solution was ACSF with green (A10436, Thermo Fisher Scientific) or red (A10438, Thermo Fisher Scientific) fluorescent dye (20 µM). At the end of recording, the membrane was ruptured to fill the recorded cell. Signals were passed through the DigiData 1440A system and amplified using the Multiclamp 700B amplifier, and recorded using the pClamp software (v.11, Molecular Devices). After initial spontaneous firing of 10 min, the excitability of the local circuit was increased with bath application of high extracellular K^+ concentration (9 mM) and/or a broad inhibitor of voltage-gated potassium, 4-aminopyridine (100 µM). Detection of action potentials was performed in Spike2 (v.7.10c, Cambridge Electronic Design) and further data analysis was performed in MATLAB (R2021b, MathWorks).

Histology

Mice were deeply anaesthetized with isoflurane overdose and transcardially perfused with 10% sucrose in Milli-Q water, followed by ice-cold 4% paraformaldehyde in 0.1 M phosphate buffer, pH 7.4. The brains were dissected and post-fixed in the same fixative overnight at 4 °C and freeze-protected in 30% sucrose in phosphate-buffered saline (PBS) at 4 °C until they sank. The brains were embedded in OCT compound (Sakura Finetek) and frozen in dry-ice-cooled ethanol.

For monosynaptic rabies virus tracing, 80 µm free-floating coronal sections were made using a cryostat (Leica Biosystems). The sections were briefly washed in PBS and stained with Neurotrace Blue fluorescent Nissl stain (1:500, Thermo Fisher Scientific, N21479) in 0.3% Triton X-100/PBS overnight at 4 °C. The sections were briefly rinsed with PBS and mounted on slides with Mowiol.

Free-floating FISH was performed as described previously[46]. Free-floating coronal sections (60 µm) containing the vIRt area were incubated in 0.3% Triton X-100/DEPC-treated PBS (DEPC-PBS) at room temperature for 20 min. After washing in PBS, the sections were incubated in proteinase K/DEPC-PBS (5 µg ml^{-1}) for 30 min at 37 °C. The sections were then acetylated for 10 min. After washing in DEPC-PBS, the sections were incubated in hybridization buffer (5× SSC, 2% blocking reagent (Sigma-Aldrich, 11096176001), 50% formamide (Thermo Fisher Scientific, AM9342), 0.1% *N*-lauroylsarcosine (NLS, Sigma-Aldrich, 61743), 0.1% SDS (Sigma-Aldrich, 71736)) for 3 h at 60 °C. The sections were then incubated with *GlyT2* probe (denatured in hybridization buffer at 80 °C for 5 min and snap-cooled on ice for 5 min, 1:1,000)[28] in the hybridization buffer overnight at 60 °C. The sections were then washed in a series of wash buffers (2× SSC, 50% formamide and 0.1% NLS at 60 °C; 2× SSC and 0.1% NLS at 37 °C; and 0.2× SSC and 0.1% NLS at 37 °C, twice for 15 min for each wash buffer). The sections were washed in 0.1% Triton X-100/TBS (TBST) for 5 min and blocked in 10% Blocking One (Nacalai, 03953-95)/TBST for 1 h at room temperature. The sections were incubated with sheep anti-DIG-AP (1:3,500, Sigma-Aldrich, 11093274910) and rabbit anti-GFP (1:1,000, Abcam, ab290) antibodies overnight at 4 °C. After washing in TBST (three times for 15 min), the sections were incubated in 100 mM Tris-HCl (pH 8.0) for 5 min and then incubated with Fast Red (SIGMAFAST, Sigma-Aldrich, F4648) for 90 min at room temperature to develop the *GlyT2* signal. After rinsing in TBST, the sections were incubated with Donkey anti-rabbit-IgG Alexa Fluor 488 (1:500, Jackson ImmunoResearch, 711-545-152) and DAPI overnight at 4 °C. After washing in TBST, the sections were mounted onto slides with Mowiol.

HCR (v.3.0) RNA-FISH was performed using reagents from Molecular Instruments. Free-floating coronal sections (60 µm) were pretreated according to a previously described method[51] with slight modifications. In brief, the sections were incubated in 70% Ethanol/PBS overnight at 4 °C. After washing in DEPC-PBS (twice for 3 min), the sections were treated with 5% SDS/DEPC-PBS for 45 min at room temperature. After rinsing in 2× SSC, the sections were incubated in 2× SSC for 15 min. The sections were then incubated in probe hybridization buffer for 30 min at 37 °C for 30 min, followed by incubation with a combination of *PV, vGlut2* and *vGat* probes (Molecular Instruments) overnight at 37 °C. After washing in HCR probe wash buffer (four times for 15 min at 37 °C), the sections were rinsed in 2× SSC (twice for 5 min) and incubated in HCR amplification buffer for 30 min at room temperature. The sections were then incubated for 48 hours at 25 °C with appropriate hairpins

conjugated with Alexa Fluor 546 or 647 (denatured and snap-cooled according to manufacturer's instructions) to visualize hybridization signals. After washing in 2× SSC (twice for 5 min), the sections were counterstained with DAPI and mounted on slides with Mowiol.

For the molecular characterization of pre-vIRt$_{PV}$ neurons, TVA–mCherry protein was detected by HCR immunohistochemistry (IHC) together with *PV*, *vGat* and *vGlut2* mRNA. In brief, after pretreatment with 70% ethanol/PBS and 5% SDS/DEPC-PBS, the sections were incubated with rabbit anti-RFP antibodies (1:2,000, Rockland, 600-401-379) and then incubated with donkey anti-rabbit antibodies conjugated to an initiator for B4 amplifier (1:2000, Molecular Instruments). After fixation with 4% PFA/PBS, the sections were processed for HCR RNA-FISH as described above. After hybridization, HCR IHC and HCR RNA-FISH signals were visualized with the appropriate hairpins conjugated to Alexa Fluor 546 or 647. Owing to constraints of spectral flexibility of the confocal microscope, *PV* and TVA–mCherry were visualized with the same fluorophore. *PV* HCR RNA-FISH only visualizes cell bodies. On the other hand, TVA–mCherry HCR IHC stains axons and dendrites as well as cell bodies as TVA–mCherry is a membrane protein. Thus, pre-vIRt$_{PV}$ neurons (GFP$^+$TVA–mCherry$^-$) were distinguished from source cells (GFP$^+$PV$^+$TVA–mCherry$^+$) by their lack of grey-colour-labelled (pseudocolour for *PV* and TVA–mCherry) axons/dendrites.

Immunostaining

Anti-gephyrin staining was performed after the GFE3 experiment. Free-floating coronal sections (25 µm) containing the vIRt area were processed using the SHIELD post-fixation protocol[52] according to the manufacturer's instruction (LifeCanvas Technologies). In brief, the sections were incubated in SHIELD-OFF solution for 24 h at 4 °C, followed by incubation in SHIELD-ON buffer for 24 h at 37 °C. The sections were then delipidated in passive clearing solution (LifeCanvas Technologies) for 24 h at 42 °C. After washing in PBS, the sections were immunostained for gephyrin and GFP using a standard immunostaining method.

The antibodies used included rabbit anti-gephyrin (1:500, Synaptic Systems, 147008), chicken anti-GFP (1:1,000, Aves labs, GFP-1010), donkey anti-rabbit-Alexa Fluor 555 (1:500, Thermo Fisher Scientific, A32794), and donkey anti-chicken Alexa Fluor 488 (1:500, Jackson ImmunoResearch, 703-545-155). The sections were counterstained with Neurotrace Blue and mounted on slides with Mowiol.

Confocal imaging

Histological images were acquired using the LSM700 (Zeiss) confocal microscope.

Three-dimensional reconstruction of the pre-vIRt$_{PV}$ circuit

Registration of pre-vIRt$_{PV}$ neurons in the Allen Mouse Brain Common Coordinate Framework (CCFv3)[27] was performed as described previously[10]. The coordinates of registered neurons were converted into Allen CCF coordinates as follows. AP, ML and DV coordinates were multiplied by 1,000, and then 5,400 and 5,700 were added to AP and ML coordinates, respectively. After the conversion, the neurons were visualized using Brainrender[53].

Spatial correlation analysis

The multivariate kernel smoothing density estimation was applied (bandwidth = 1) to the (x,y,z) coordinates of each cell. The resulting kernel density estimation was then vectorized, and the cosine similarity between any two of the mice was calculated to form the correlogram. The coordinates of vibrissa premotor neurons were derived from a previously published work[10].

Analysis of gephyrin-positive synapses

For counting gephyrin-positive synapses, sections were immunostained as described above and imaged using the LSM700 system using a ×40 objective lens with ×1.5 zoom. Gephyrin-positive synapses localizing on the cell perimeter of optically sectioned neurons were counted. The number of synapses on each neuron was normalized by dividing by the cell perimeter measured in ImageJ.

Spike data analysis

Spike sorting was performed using Kilosort2 (ref. [54]) with final curation performed using JRClust[55]. Responsivity to laser pulses (opto-tagging) was quantified using the stimulus-associated spike latency test (SALT[56]). Cells were classified as tuned to the whisking phase according to three statistical measures: first we measured the spike/phase coherence for each whisking epoch using a multitaper spectral estimation method (Chronux; http://chronux.org/) and computed the confidence level for $P = 0.01$. We then compared the distribution of spike-occurring whisking phases with the overall distribution of whisking phases (Kuiper two-sample test, $P = 0.05$, CircStat[57]). From these distributions, we calculated the probability of spiking according to the whisking phase. Finally, we performed further circular statistics to assess the phase tuning of each neuron (Rayleigh test for non-uniformity of circular data, $P = 0.05$, CircStat) and obtained descriptive statistics of the periodic activity pattern (CircStat). We also set a minimum whisking epoch duration of 3 s. For each recording, data for epochs that did not meet all of those criteria were discarded. Phase-tuned cells were grouped according to their peak coherence phase (PCP) according to these arbitrary limits: retraction units: PCP ≥ −30 and <65; mid-retraction units: PCP ≥ 65 and <150; protraction units: PCP ≥ 150 and <−115; mid-protraction units: PCP ≥ −115 and <−30. Cells were also classified between fast and slow rhythmic activity, to separate those mainly implicated in whisking from those concerned with slower oscillations such as changes in vibrissa midpoint or breathing. To do so, we computed the power spectral density between 3 and 20 Hz (multitaper spectrum, Chronux) to obtain the median spiking frequency. Cells with a median frequency of below 9 Hz were classified as slow rhythmic.

Vibrissa tracking and computation of whisking parameters

Vibrissa kinematics were obtained with homemade data processing pipelines based on Janelia Whisker Tracker (Whisk[58]). The videography processing pipeline provided a set of vibrissa coordinates for each video frame from which whisking parameters (such as angle, velocity, midpoint, amplitude) were subsequently obtained. Whisking phase was calculated from the angle trace, band-pass filtering the trace between 8 Hz and 30 Hz (three-pole Butterworth filter run in forward and backward directions), and applying the Hilbert transform[7,59]. Whisking parameters were related as: $\theta_{whisk}(t) = \theta_{midpoint} - \theta_{amp}[1 + \cos(2\pi f_{whisk}(t) - \phi_0)]$, with θ_{whisk} the absolute angle, f_{whisk} the instantaneous whisking frequency and ϕ_0 the phase at the peak spike rate in the whisking cycle. Individual whisks (or, similarly, breathing) cycles were identified by phase resets of the Hilbert transform. A vibrissal motion was identified as protraction or retraction onset if the phase value exceeded ±3.

Power spectrum analysis of whisking traces

Raw vibrissa angles were band-pass filtered (fourth order Butterworth) with low- and high-frequency cut-offs of 5 and 30 Hz, respectively. A Welch transform was used to calculate the time average spectrogram of the vibrissa signal with the following parameters: nfft = 512, window = 102, overlap = 101 and sampling frequency = 500 Hz. For experiments with trial structure (TeLC, GtACR2 and NpHR3.3 silencing), spectrograms were averaged across animals and trials. GFE3 inhibitory synapse ablation experiments did not have trials, so spectrograms were calculated from the entire experiment duration, and then averaged across animals. The controls for TeLC silencing were vibrissae on the contralateral side; the controls for GFE3-inhibitory synapse ablation experiments were a separate group of GFP animals; and the controls for the GtACR2 optogenetic silencing experiments were the same vibrissae whisking in the air during the period before laser illumination. Breathing sensor analysis was mostly the same, except that the output of the sensor was first low-pass

filtered with a cut-off frequency of 500, and then downsampled from a sampling rate of 30,000 Hz to 500 Hz. Then, the band-pass filter before Welch transform used cut-off frequencies of 1 Hz and 15 Hz.

State-transition analysis

The recorded raw whisking angles of a single mouse was first corrected by subtracting the midpoint trace from the raw whisking angles. The processed whisking angle trace was then evenly divided and binned into finite states ($n = 100$) on the basis of the whisking angle (0.02–99.8% of the whisking angle range). Then, for each time point t, we extracted the state i.d. s_t and the state i.d. s_{t+1} of the next time point $t + 1$, then the number of the transition from s_t to s_{t+1} was added one. For all of the time points, we calculated how many times the states transitioned from a state s_i to s_j and formed this two-dimensional histogram into a matrix showing the overall state transitions between each other.

Similarity score

To get the initial similarity between the whisking and breathing patterns in both the control and GFE3 mice, we calculated the similarity score by computing the correlation coefficient between the whisking angle (midpoint corrected) and the breathing signal.

Coherence between whisking and breathing

To investigate the whisking components other than those directly coupled to the breathing, we calculated the magnitude-squared coherence between the whisking and breathing signals. The coherence measures the squared correlation coefficient of the cross-spectrum density functions of the signals with the frequency range 0.5–20 Hz. To get the overall oscillation pattern, we calculated the averaged coherence with s.e.m. for all of the control and GFE3 mice.

Statistics

Levels of significance are shown as follows: $^{*}P \leq 0.05$, $^{**}P \leq 0.01$. The data were tested for normality using quantile plots and/or Shapiro–Wilk normality tests in Prism. Data with non-normal distributions were compared using nonparametric tests. The following statistical tests were used. Figure 1m: quantification of whisking amplitude (control versus vIRt$_{PV}$-TeLC): $P = 0.0286$, Kolmogorov–Smirnov (KS) test. Figure 1n: quantification of whisking midpoint (control versus vIRt$_{PV}$-TeLC): $P = 0.0286$, Kolmogorov–Smirnov test. Figure 4c: quantification of normalized density of gephyrin puncta on GFE3-positive vIRt$_{PV}$ neurons and neighbouring neurons: $P = 0.0286$, Kolmogorov–Smirnov test. Figure 4f: quantification of whisking and breathing parameters (control versus vIRt$_{PV}$-GFE3). Whisking amplitude: $P = 0.0047$, Kolmogorov–Smirnov test. Whisking midpoint: $P = 0.58$, Kolmogorov–Smirnov test. Breathing duty cycle: $P = 0.53$, Kolmogorov–Smirnov test. Figure 4g: quantification of the number of whisks per one breathing cycle. vIRt$_{PV}$-GFE3 (1 whisk per breath) versus vIRt$_{PV}$-GFE3 (2 whisks per breath): $P = 0.0156$, Wilcoxon matched-pairs signed-rank tests. Figure 4j: correlation coefficient of breathing and whisking (control versus vIRt$_{PV}$-GFE3): $P = 0.0082$, Kolmogorov–Smirnov test. Extended Data Figure 1i: quantification of whisking amplitude (vIRt$_{vGlut2}$-NpHR3.3, laser off versus laser on): $P = 0.8438$, Wilcoxon matched-pairs signed-rank tests. Extended Data Figure 1j: quantification of whisking midpoint (vIRt$_{vGlut2}$-NpHR3.3, laser off versus laser on): $P = 0.1562$, Wilcoxon matched-pairs signed-rank tests. Extended Data Figure 2f: quantification of whisking amplitude (vIRt$_{PV}$-GtACR2, laser off versus laser on): $P = 0.0312$, Wilcoxon matched-pairs signed-rank tests.

Reporting summary

Further information on research design is available in the Nature Research Reporting Summary linked to this article.

Data availability

The data are available from the corresponding authors on reasonable request. Source data are provided with this paper.

Code availability

Custom-made scripts used in this Article are available at GitHub (https://github.com/wanglab-neuro/the-whisking-oscillator-circuit).

45. Mattis, J. et al. Principles for applying optogenetic tools derived from direct comparative analysis of microbial opsins. *Nat. Methods* **9**, 159–172 (2011).
46. Stanek, E. 4th, Rodriguez, E., Zhao, S., Han, B. X. & Wang, F. Supratrigeminal bilaterally projecting neurons maintain basal tone and enable bilateral phasic activation of jaw-closing muscles. *J. Neurosci.* **36**, 7663–7675 (2016).
47. Rodriguez, E. et al. A craniofacial-specific monosynaptic circuit enables heightened affective pain. *Nat. Neurosci.* **20**, 1734–1743 (2017).
48. Sakurai, K. et al. Capturing and manipulating activated neuronal ensembles with cane delineates a hypothalamic social-fear circuit. *Neuron* **92**, 739–753 (2016).
49. Petreanu, L., Mao, T., Sternson, S. M. & Svoboda, K. The subcellular organization of neocortical excitatory connections. *Nature* **457**, 1142–1145 (2009).
50. Lopes, G. et al. Bonsai: an event-based framework for processing and controlling data streams. *Front. Neuroinform.* **9**, 7 (2015).
51. Nicovich, P. R. et al. Multimodal cell type correspondence by intersectional mFISH in intact tissues. Preprint at *bioRxiv* https://doi.org/10.1101/525451 (2019).
52. Park, Y. G. et al. Protection of tissue physicochemical properties using polyfunctional crosslinkers. *Nat. Biotechnol*. https://doi.org/10.1038/nbt.4281 (2018).
53. Claudi, F. et al. Visualizing anatomically registered data with brainrender. *eLife* **10**, e65751 (2021).
54. Pachitariu, M., Steinmetz, N., Kadir, S., Carandini, M. & Kenneth, D. H. Kilosort: realtime spike-sorting for extracellular electrophysiology with hundreds of channels. Preprint at *bioRxiv* https://doi.org/10.1101/061481 (2016).
55. Jun, J. J. et al. Real-time spike sorting platform for high-density extracellular probes with ground-truth validation and drift correction. Preprint at *bioRxiv* https://doi.org/10.1101/101030 (2017).
56. Kvitsiani, D. et al. Distinct behavioural and network correlates of two interneuron types in prefrontal cortex. *Nature* **498**, 363–366 (2013).
57. Berens, P. CircStat: a MATLAB toolbox for circular statistics. *J. Stat. Softw.* **31**, 1–21 (2009).
58. Clack, N. G. et al. Automated tracking of whiskers in videos of head fixed rodents. *PLoS Comput. Biol.* **8**, e1002591 (2012).
59. Aljadeff, J., Lansdell, B. J., Fairhall, A. L. & Kleinfeld, D. Analysis of neuronal spike trains, deconstructed. *Neuron* **91**, 221–259 (2016).

Acknowledgements We thank the members of the Wang laboratory and the aABC U19 BRAIN Circuit Team for discussions and suggestions; B.-X. Han and S. Choi for mouse colony maintenance; and staff at the Boston Children's Hospital Viral Core for the production of AAV2retro-CAG-Cre. This work is supported by NIH grants U19 NS107466 and R01 NS077986.

Author contributions J.T., V.P. and F.W. conceptualized the project, designed experiments and wrote the paper with input from all of the authors. J.T. and V.P. performed the majority of the experiments with help from J.L., P.M.T. and S.L.; L.C. performed slice electrophysiology with crucial support from Z.H.; J.T., V.P., J.L. and P.M.T. analysed data. S.Z. and A.H. produced several viral vectors. D.G. and D.K. contributed to behaviour and electrophysiology data analysis and theoretical issues, and provided help with the intra-aural illumination opto-tagging. F.W. supervised all of the work.

Competing interests The authors declare no competing interests.

Additional information

Supplementary information The online version contains supplementary material available at https://doi.org/10.1038/s41586-022-05144-8.

Correspondence and requests for materials should be addressed to Jun Takatoh or Fan Wang.

Peer review information *Nature* thanks Jan Marino Ramirez and the other, anonymous, reviewer(s) for their contribution to the peer review of this work. Peer reviewer reports are available.

Reprints and permissions information is available at http://www.nature.com/reprints.

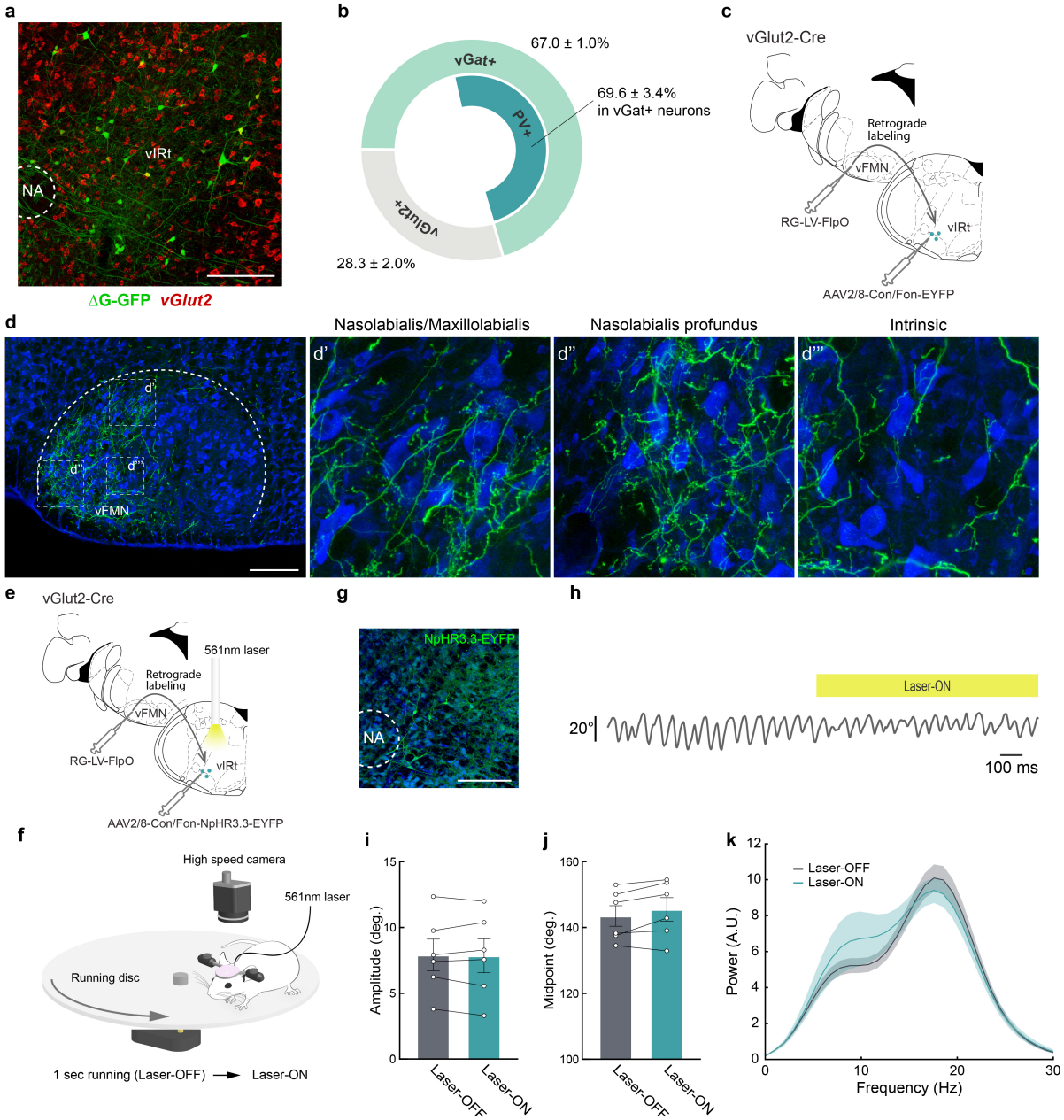

Extended Data Fig. 1 | Anatomical and functional characterization of vIRt$_{vGlut2}$ neurons. a, Representative image of vibrissa premotor neurons (green) in vIRt traced by a three-step monosynaptic rabies virus tracing method shown in Fig. 1. *vGlut2* (red) mRNA were visualized by HCR RNA-FISH. **b**, Molecular identity of premotor vIRt neurons. 67.0 ± 1.0% (n = 4) and 22.8 ± 1.3% (n = 3) of premotor vIRt neurons are vGat$^+$ and vGlut2$^+$, respectively. 69.6 ± 3.4% (n = 4) of vGat$^+$ premotor vIRt neurons are PV$^+$. **c**, Strategy for labelling vGlut2$^+$ premotor vIRt neurons (vIRt$_{vGlut2}$). Retrograde lentivirus carrying FlpO (RG-LV-FlpO) and AAV carrying Cre- and Flp-dependent-EYFP (AAV2/8-Con/Fon-EYFP) are injected into the vFMN and vIRt of the vGlut2-Cre animal, respectively. **c**, Projection pattern of vIRt$_{vGlut2}$ neurons in the vFMN. **d'**,**d''**,**d'''**, High-magnification views of the boxed areas in **d**. The dorsolateral (**d'**), lateral (**d''**), and ventrolateral (**d'''**) facial motor subnuclei that contain motoneurons innervating the nasolabialis/maxillolabialis, nasolabialis profundus, and intrinsic muscles, respectively. **e**, A schematic of vIRt$_{vGlut2}$ silencing experiment. **f**, Experimental setup for vibrissa tracking. One second running triggers 1 s continuous 561 nm laser stimulation. **g**, Representative image of NpHR3.3-EYFP expression in vIRt. **h**, Example vibrissa trace during laser-OFF and -ON period. **i**, Quantification of whisking amplitude (Laser-OFF, 7.9 ± 1.2° vs. Laser-ON, 7.9 ± 1.3°, n = 6, p = 0.8438, Wilcoxon signed-rank test). **j**, Quantification of whisking midpoint (Laser-OFF, 53.5 ± 3.1° vs. Laser-ON, 55.5 ± 3.5°, n = 6, p = 0.1562, Wilcoxon signed-rank test). **k**, Power spectrum analysis of whisking frequency in Laser-OFF and -ON period. Shaded areas are mean ± s.e.m. Data are mean ± s.e.m. Brain sections were counterstained with Neurotrace Blue (**d**, **g**).

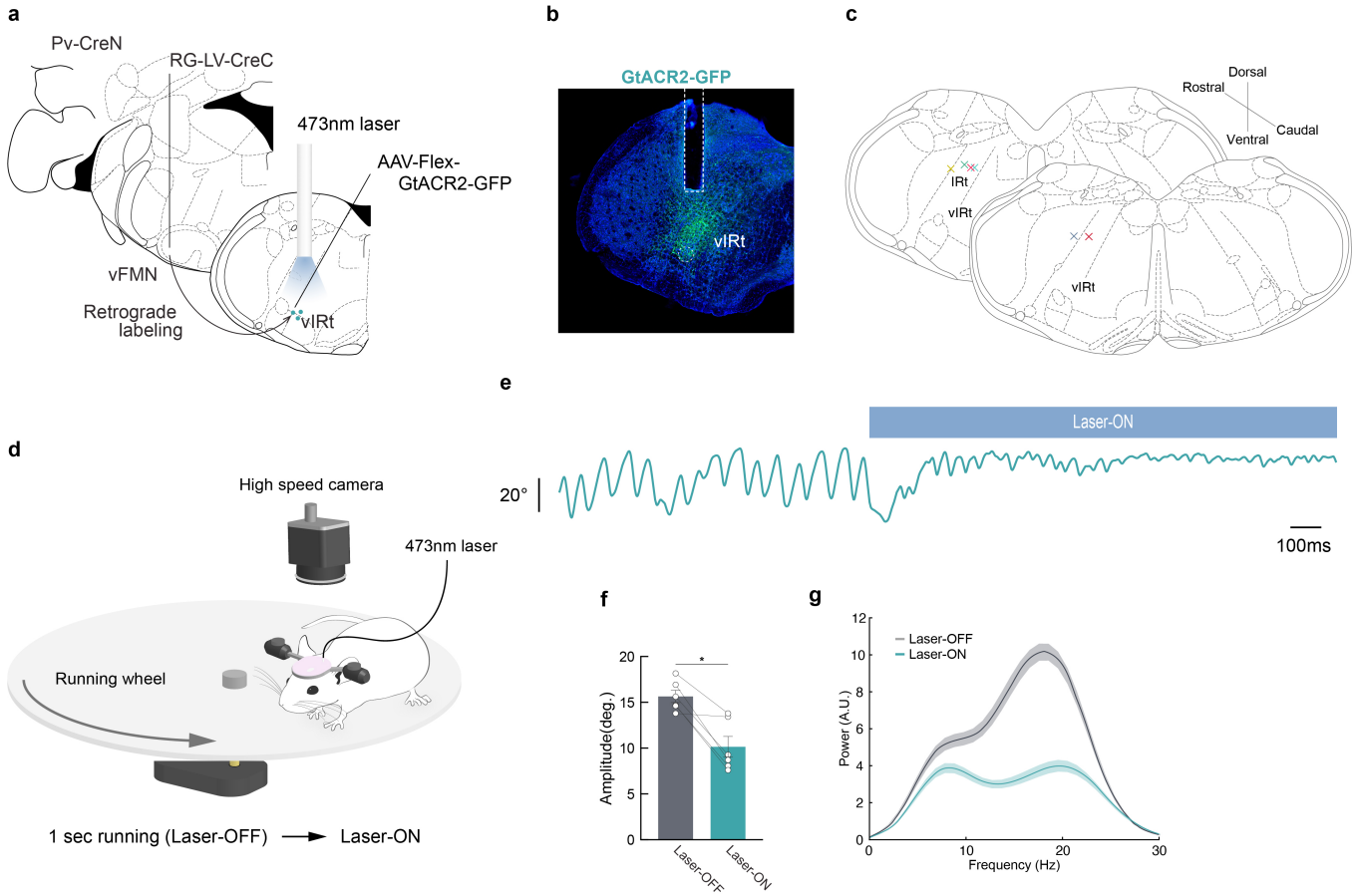

Extended Data Fig. 2 | Optogenetic silencing of vIRt$_{PV}$ neurons also impaired whisking. a, A schematic of vIRt $_{PV}$ GtACR2 silencing experiment. **b**, Representative image of GtACR2 expression and the optic fibre track. **c**, Optic fibre tip placements over vIRt from all AAV-Flex-GtACR2-GFP injected animals. **d**, Experimental setup for vibrissa tracking. One second running triggers 1 s continuous 473 nm laser stimulation. **e**, Example vibrissa trace during laser-OFF and -ON period. **f**, Quantification of whisking amplitude (Laser-OFF, 15.6 ± 0.7° vs. Laser-ON, 10.2 ± 1.1°, n = 5, p = 0.0312, Wilcoxon signed-rank test). **g**, Power spectrum analysis of whisking frequency in Laser-OFF and -ON period. Data are mean ± s.e.m. * P ≤ 0.05. Brain sections were counterstained with Neurotrace Blue (**b**).

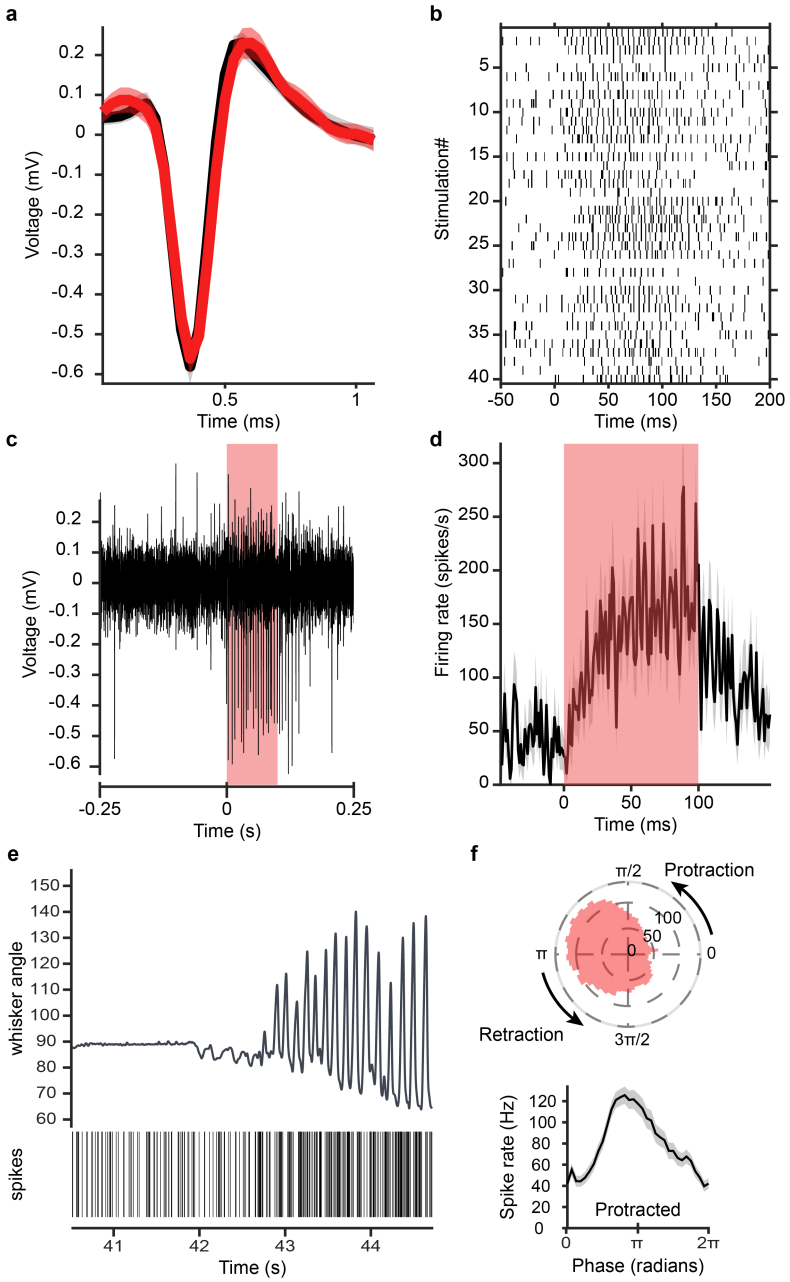

Extended Data Fig. 3 | Antidromic opto-tagging of a ChRmine-expressing vIRt$_{PV}$ neuron via light stimulation through the ear. a, Overlapped average waveform, before (black) and during (red) stimulation periods. **b**, Raster plot of spike times aligned to stimulation onset for 40 light pulses. **c**, Example single channel recording trace showing antidromic spikes from the opto-tagged unit during a light pulse. **d**, Firing rate of that unit averaged over 40 light stimulations epochs. **e**, Unit activity during transition from resting to whisking state. vibrissa angle traces for the ipsilateral C2 vibrissa. Bottom: Spike raster plot for this opto-tagged vIRt$_{PV}$-ChRmine neuron. **f**, Phase tuning. Average spike rate across whisking phases for this opto-tagged vIRt$_{PV}$-ChRmine neuron, in polar (top) and cartesian coordinates (bottom).

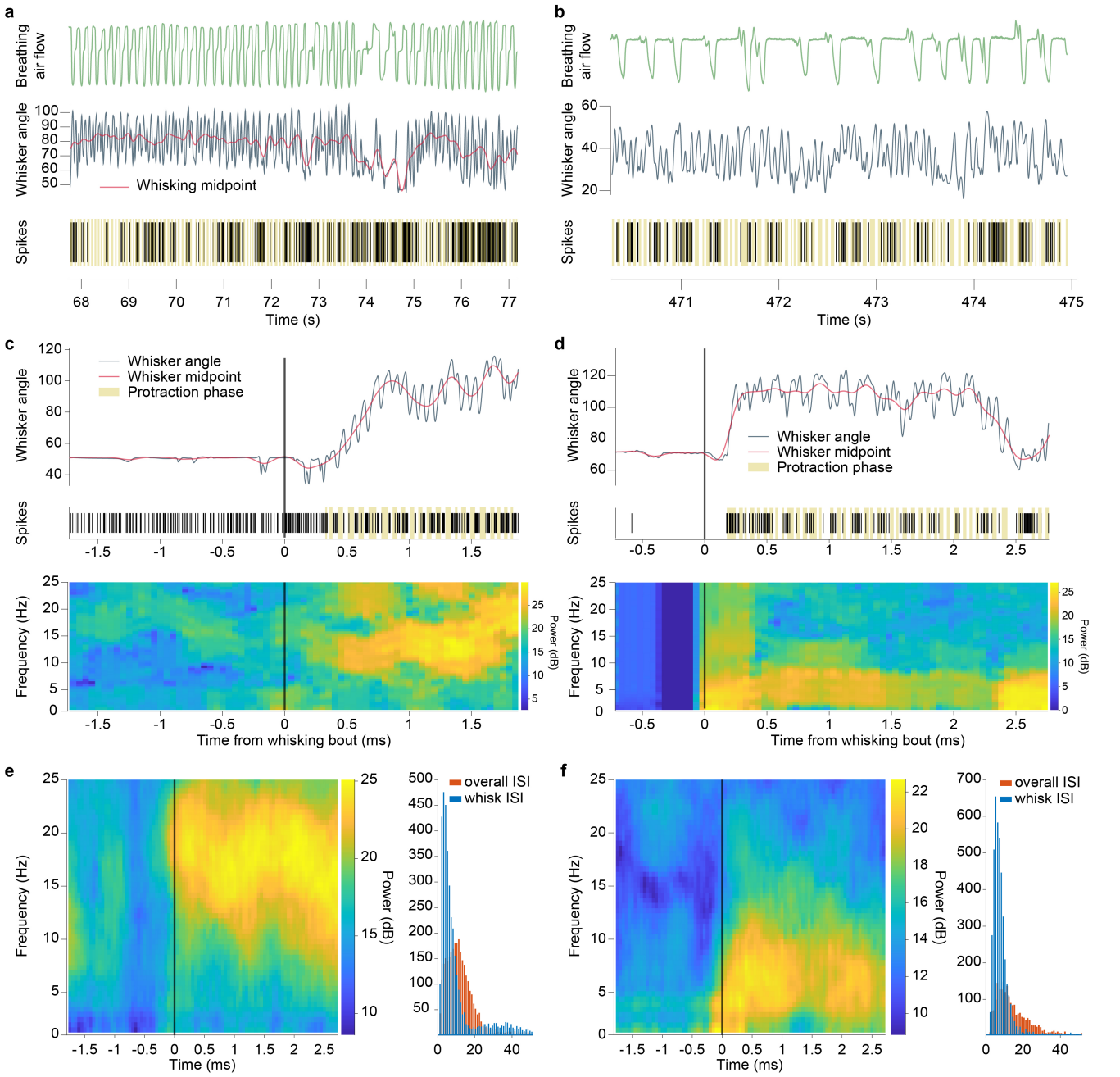

Extended Data Fig. 4 | Slow oscillation vIRt units and additional analysis of transition from tonic to rhythmic firing of vIRt units. a, **b**, Two vIRt units with "slow" rhythmic activity patterns. Top: breathing trace. Middle: Vibrissa angle and midpoint traces. Bottom: raster plot of spiking events (protraction phases shown in beige). **c**, Top: vibrissa trace and raster plot for a retraction unit. Bottom: Time-frequency spectrum of that spiking activity. The transition to rhythmic bursting appears as a high power frequency band, corresponding to whisking frequency. **d**, Same as **c**, for a "slow" oscillation unit. Here the transition to whisking shows a low frequency band, similar to vibrissa midpoint variations or breathing rhythm. **e**, Left: Time-frequency spiking spectrum for a retraction unit, averaged over all whisking bouts. Right: Inter-spike interval histograms for that retraction unit. Red, overall ISI. Blue, ISI during long whisking bouts. The ISI distribution becomes bimodal, with a strong peak at short interval corresponding to bursts. **f**, same as **e**, for a "slow" oscillation unit.

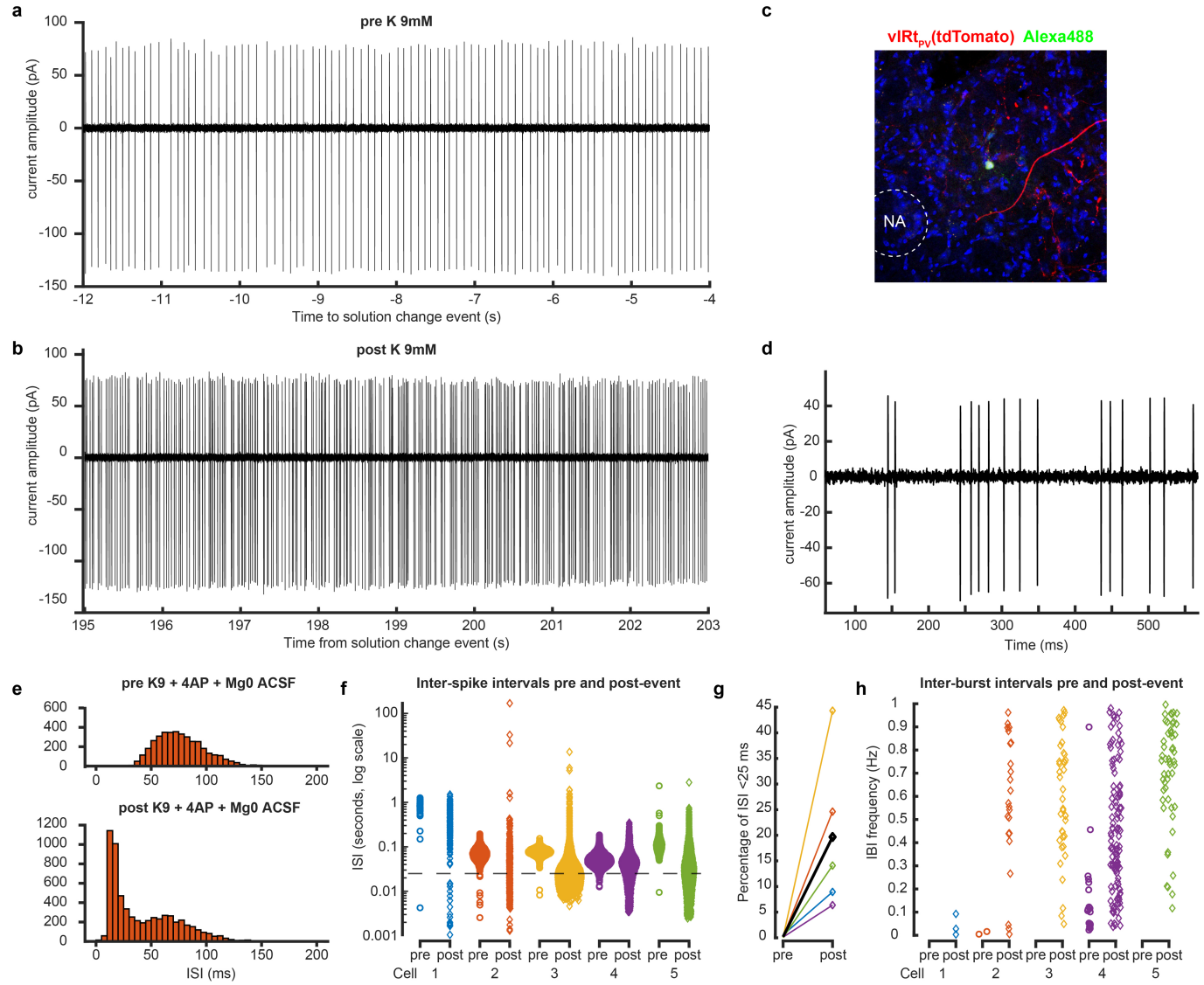

Extended Data Fig. 5 | Elevated extracellular potassium concentrations induce bursting but not rhythmic activity in vIRt$_{PV}$ neurons. **a**,**b**, Cell-attached recording of a vIRt$_{PV}$ unit before (a) and after (b) bath application of K 9 mM. **c**, Representative histological verification of targeted recording. One of the tdTomato-expressing vIRt$_{PV}$ in slice is filled with green Alexa 488 dye from the recording pipette. **d**, Example of burst, post increase of extracellular potassium concentration. **e**, **f**, Inter-spike interval distribution, pre and post increase of extracellular potassium concentration, for one cell (**e**, pre: top, post: bottom) and all cells (**f**, ISI shown in log scale. Dash line: 40 Hz). **g**, Percentage of ISIs shorter than 25 ms (i.e., above 40 Hz), pre and post event, for all cells (average shown in black). **h**, Inter-burst frequency, for each cell, pre and post. No bursting frequency band is observed for any cell.

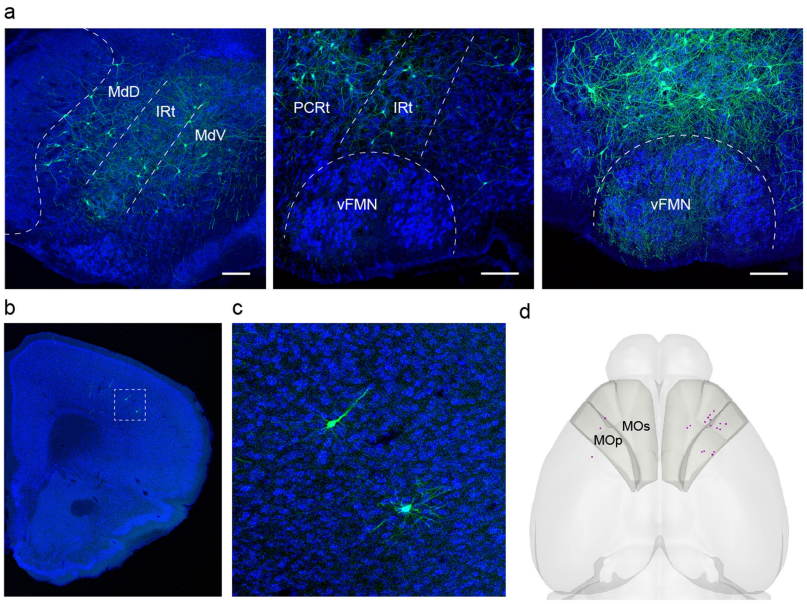

e

Nucleus		*vGat*	*vGlut2*
Superior colliculus		NA	95.4 ± 3.9% n = 4
Midbrain reticular nucleus		NA	95.4% ± 3.4%, n = 4
Deep cerebellar nucleus		NA	100%, n = 4
PreBötzinger complex		86.3 ± 1.8% n = 3	NA
Medullary reticular nucleus		96.6 ± 1.7% n = 3	NA
Intermediate reticular nucleus	Ipsi.	51.1% (97/190, n = 2)	43.2% (82/190, n = 2)
	Cont.	19.0% (27/142, n = 2)	79.6% (113/142, n = 2)
Gigantocellular reticular nucleus	Ipsi.	39.2% (51/130, n = 2)	58.5% (76/130, n = 2)
	Cont.	36.3% (37/102, n = 2)	61.8% (63/102, n = 2)

Extended Data Fig. 6 | Pre-vIRt$_{PV}$ neurons in the brainstem and motor cortex, and neurotransmitter characterization of pre-vIRt$_{PV}$ neurons. **a**, Representative image of ΔG-GFP labelled pre-vIRt$_{PV}$ neurons in the brainstem (continued from Fig. 3c). Scale bars, 200 µm. **b**, Representative image of ΔG-GFP labelled pre-vIRt$_{PV}$ neurons in the cortex. Scale bar, 500 µm. **c**, Zoomed image of the boxed area in **b**, **d**, Representative 3D reconstructed image of labelled pre-vIRt$_{PV}$ neurons in the cortex (magenta). Shaded areas denote the primary motor (MOp) and secondary motor cortices (MOs). **e**, Neurotransmitter phenotype of pre-vIRt$_{PV}$ neurons determined by fluorescent in situ hybridization or HCR RNA-FISH.

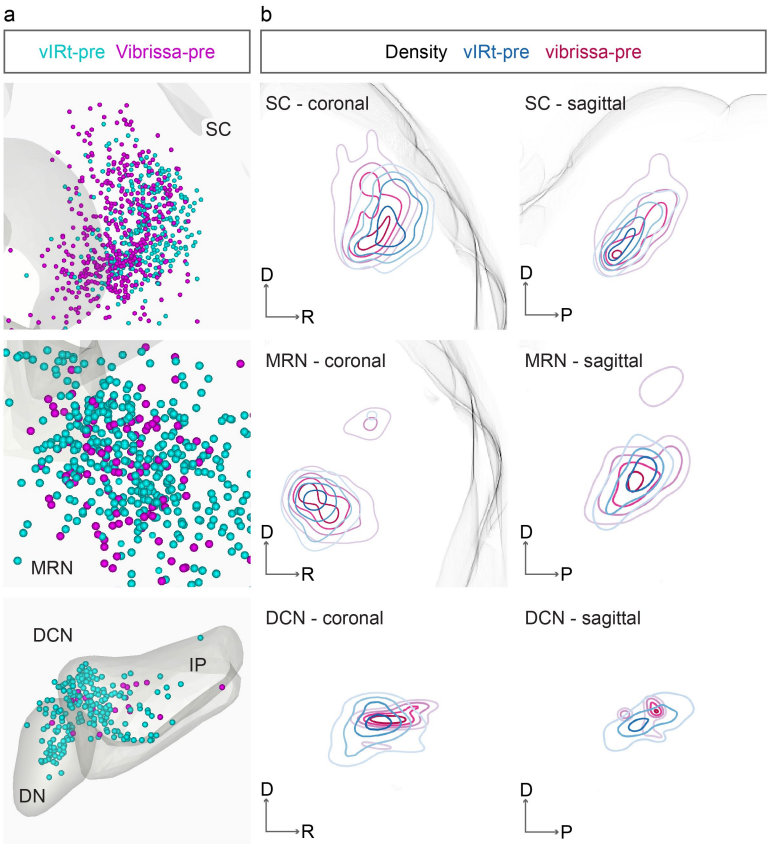

Extended Data Fig. 7 | Comparison of the distributions of vIRt$_{PV}$ presynaptic neurons and vibrissal premotor neurons. **a**, Three-dimensionally reconstructed vIRt$_{PV}$ presynaptic neurons (vIRt-pre, cyan, n = 3) and vibrissal premotor neurons (vibrissa-pre, magenta, n = 4) in the Allen Mouse Brain CCF in coronal planes. **b**, Density analysis of presynaptic neurons (vIRt-pre, cyan, n = 3) and vibrissal premotor neurons (vibrissa-pre, magenta, n = 4) in coronal and sagittal planes. DN, dentate nucleus; IP, interposed nucleus.

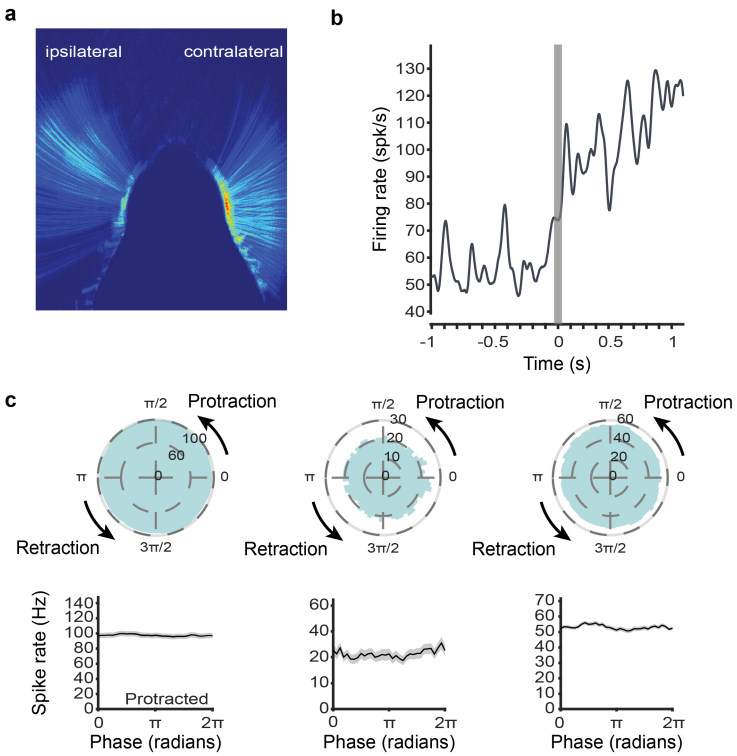

Extended Data Fig. 8 | Additional results from vIRt$_{PV}$-ChRmine-GFE3 mice. **a**, Average whisking activity of a vIRt$_{PV}$-ChRmine-GFE3 mouse, showing the mean of the pixel intensity difference between each consecutive video frame. Blue to red colour scale: low to high activity. In contrast to the ipsilateral (GFE3) side, contralateral whisking is highly active across the whole whisking range. **b**, Increased firing, but no rhythmic activity at whisking initiation for a opto-tagged vIRt$_{PV}$-ChRmine-GFE3 unit (whisking initiation time determined from contralateral C2 vibrissa). **c**, Whisking phase tuning of all opto-tagged vIRt$_{PV}$-ChRmine-GFE3 single units (conventions as in Figs. 2 and 4).

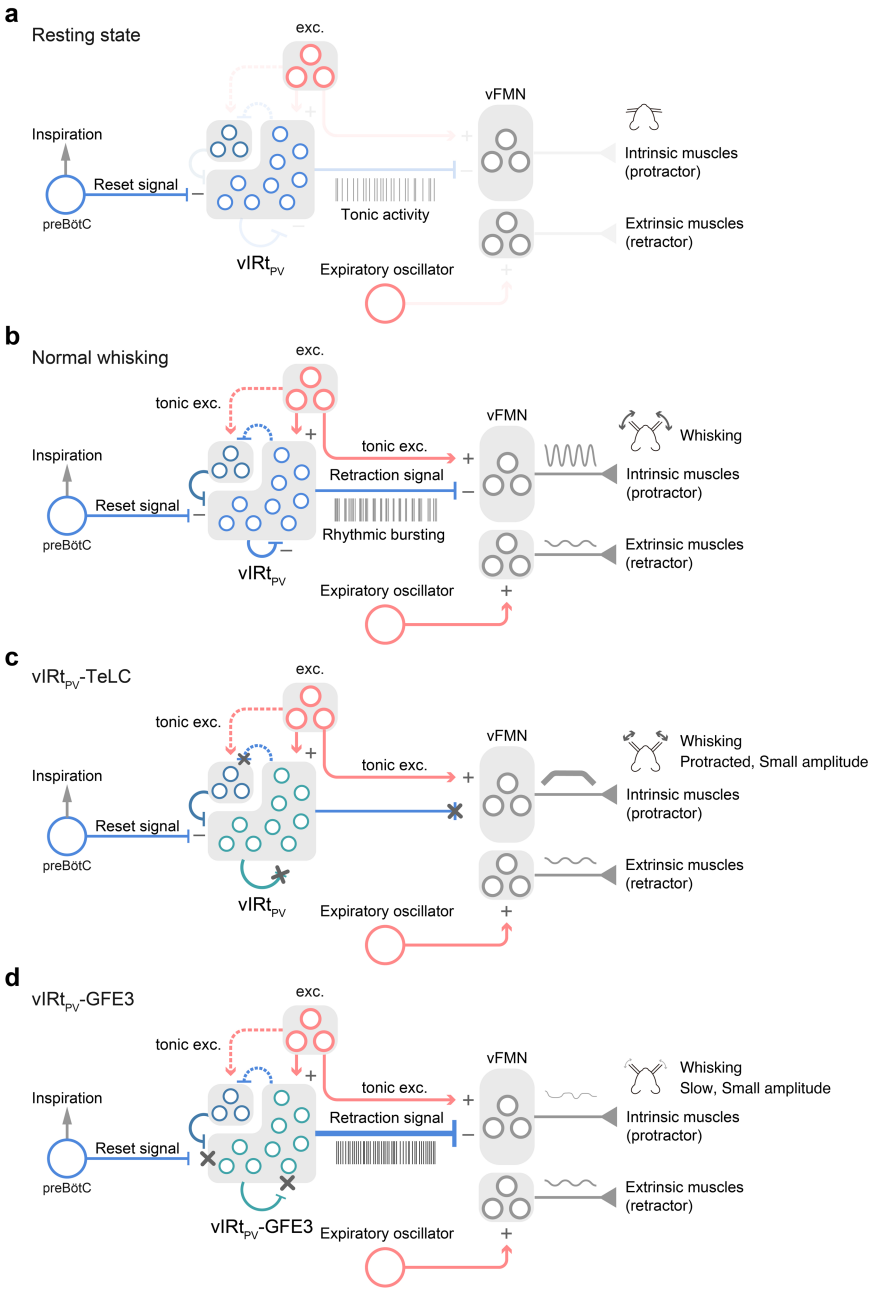

Extended Data Fig. 9 | Schematic model of the vIRt$_{PV}$ circuit that generates rhythmic whisking in normal and experimental conditions. a, In Resting state, vIRt$_{PV}$ neurons show unsynchronized tonic activity. **b**, In Normal whisking condition, tonic excitatory inputs to vFMN protractor motoneurons protract vibrissae. Concurrently, tonic excitatory inputs to vIRt$_{PV}$ neurons induce recurrent inhibition within vIRt$_{PV}$ and which in turn switches vIRt$_{PV}$ from tonic firing to synchronized rhythmic bursting mode. The rhythmic signal from vIRt$_{PV}$ periodically silences vFMN protractor motoneurons and leads to rhythmic whisking. The rhythmic inhibitory signal from the inspiratory rhythm generator preBötC resets the activity of vIRt$_{PV}$. The expiratory oscillator activates vFMN retractor motoneurons. **c**, In vIRt$_{PV}$-TeLC condition, outputs from vIRt$_{PV}$ are abolished. Lack of inhibition from vIRt$_{PV}$ results in strong continuous activation of vFMN protractor motoneurons and strong protraction of vibrissae. Because of the strong tonic activity of protractor intrinsic muscles, extrinsic retractor muscles play a minor role in vibrissa movement. **d**, In vIRt$_{PV}$-GFE3 condition, tonic excitation induces strong unsynchronized tonic inhibitory outputs from vIRt$_{PV}$ to vFMN protractor motoneurons, which results in a less protracted midpoint compared with vIRt$_{PV}$-TeLC's. Under this condition, the contribution of expiratory oscillator-extrinsic retractor muscles becomes pronounced. A group of inhibitory neurons in the left top corner of vIRt indicates PV^{-}/vGat^{+} vIRt neurons. Dotted lines denote putative connections.

nature research

Corresponding author(s): Jun Takatoh
Fan Wang

Last updated by author(s): 2022/06/27

Reporting Summary

Nature Research wishes to improve the reproducibility of the work that we publish. This form provides structure for consistency and transparency in reporting. For further information on Nature Research policies, see our Editorial Policies and the Editorial Policy Checklist.

Statistics

For all statistical analyses, confirm that the following items are present in the figure legend, table legend, main text, or Methods section.

n/a	Confirmed	
☐	☒	The exact sample size (*n*) for each experimental group/condition, given as a discrete number and unit of measurement
☐	☒	A statement on whether measurements were taken from distinct samples or whether the same sample was measured repeatedly
☐	☒	The statistical test(s) used AND whether they are one- or two-sided *Only common tests should be described solely by name; describe more complex techniques in the Methods section.*
☐	☒	A description of all covariates tested
☐	☒	A description of any assumptions or corrections, such as tests of normality and adjustment for multiple comparisons
☐	☒	A full description of the statistical parameters including central tendency (e.g. means) or other basic estimates (e.g. regression coefficient) AND variation (e.g. standard deviation) or associated estimates of uncertainty (e.g. confidence intervals)
☐	☒	For null hypothesis testing, the test statistic (e.g. *F*, *t*, *r*) with confidence intervals, effect sizes, degrees of freedom and *P* value noted *Give P values as exact values whenever suitable.*
☒	☐	For Bayesian analysis, information on the choice of priors and Markov chain Monte Carlo settings
☒	☐	For hierarchical and complex designs, identification of the appropriate level for tests and full reporting of outcomes
☒	☐	Estimates of effect sizes (e.g. Cohen's *d*, Pearson's *r*), indicating how they were calculated

Our web collection on statistics for biologists contains articles on many of the points above.

Software and code

Policy information about availability of computer code

Data collection	Python (3.8), Julia (1.5), Cereplex Direct (Blackrock Microsystems), Bonsai (bonsai-rx.org), FFmpeg (ffmpeg.org)
Data analysis	Matlab (R2019a, R2021b), Python (3.8). Custom codes including a Datajoint pipeline are available on Github.

For manuscripts utilizing custom algorithms or software that are central to the research but not yet described in published literature, software must be made available to editors and reviewers. We strongly encourage code deposition in a community repository (e.g. GitHub). See the Nature Research guidelines for submitting code & software for further information.

Data

Policy information about availability of data

All manuscripts must include a data availability statement. This statement should provide the following information, where applicable:

- Accession codes, unique identifiers, or web links for publicly available datasets
- A list of figures that have associated raw data
- A description of any restrictions on data availability

All raw data described in this study will be made available from the corresponding authors upon request. Access to the electrophysiological data can be provided through the Datajoint database.

Field-specific reporting

Please select the one below that is the best fit for your research. If you are not sure, read the appropriate sections before making your selection.

☒ Life sciences ☐ Behavioural & social sciences ☐ Ecological, evolutionary & environmental sciences

For a reference copy of the document with all sections, see nature.com/documents/nr-reporting-summary-flat.pdf

Life sciences study design

All studies must disclose on these points even when the disclosure is negative.

Sample size	Sample sizes were determined based on previous publications and common practice in animal behavior experiments.
Data exclusions	We confirmed viral expression, site of injection, insertion of optical fiber and probes through post-hoc histological analysis. The animals that showed failed expression or off target optical fiber / probe placement were excluded from further analyses.
Replication	Functional manipulation, anatomical and electrophysiological results were replicated across animals.
Randomization	Animals were randomly selected from each litter. Random group allocation was maintained throughout the study, within constraints set by availability of in-house, purpose-bred lines.
Blinding	For experiments with a control group, investigators were blinded to group allocation during data analysis.

Reporting for specific materials, systems and methods

We require information from authors about some types of materials, experimental systems and methods used in many studies. Here, indicate whether each material, system or method listed is relevant to your study. If you are not sure if a list item applies to your research, read the appropriate section before selecting a response.

Materials & experimental systems

n/a	Involved in the study
☐	☒ Antibodies
☒	☐ Eukaryotic cell lines
☒	☐ Palaeontology and archaeology
☐	☒ Animals and other organisms
☒	☐ Human research participants
☒	☐ Clinical data
☒	☐ Dual use research of concern

Methods

n/a	Involved in the study
☒	☐ ChIP-seq
☒	☐ Flow cytometry
☒	☐ MRI-based neuroimaging

Antibodies

Antibodies used	Primary antibodies: Rabbit Anti-Parvalbumin; abcam (ab11427, lot GR32847 38-2). Rabbit Anti-RFP; Rockland (600-401-379, Lot 39707). Chicken Anti-GFP; Aves labs (GFP-1010, Lot, GFP697986). Rabbit Anti-gephyrin; Synaptic systems (147 008, Lot 1-7). Secondary antibodies: Donkey anti-rabbit -IgG Alexa Fluor 488 (1:500, Jackson ImmunoResearch, 711-545-152). Donkey anti-rabbit IgG Alexa Fluor 555 (1:500, Thermo Fisher Scientific, A32794). Anti-chicken Alexa Fluor 488 (1:500, Jackson ImmunoResearch, 703-545-155). Anti-rabbit conjugated with an initiator for B4 amplifier (Molecular Instruments)
Validation	Anti-Parvalbumin; Omission of the primary antibody does not show any immunoreactive signals. Anti-RFP; This antibody does not show any immunoreactive signals against non-RFP expressing tissues. Anti-GFP; This antibody does not show any immunoreactive signals against non-GFP expressing tissues. Anti-gephyrin; This antibody does not show any immunoreactive signals in gephyrin knock-out animals.

Animals and other organisms

Policy information about studies involving animals; ARRIVE guidelines recommended for reporting animal research

Laboratory animals	40 PV-CreN knock-in, 3 Pv-CreN;Ai14 (JAX # 007914, Jackson Laboratory), 28 C57/BL6 (Jackson Laboratory) and 6 vGlut2-Cre knock-in mice (JAX #028863, Jackson Laboratory) were used in this study. Equal number of female and male mice are randomly distributed to different experiments. All animals except for 3 C57B/L6 mice, which were used for a three step RV tracing and had the first viral

	injection at P14, were used at age > P60.
Wild animals	This study did not involve wild animals.
Field-collected samples	This study did not involve field-collected samples.
Ethics oversight	All animal handling and experiment procedures were approved by The Duke University Institutional Animal Care and Use Committee (protocol # A143-18-06) and MIT Committee for Animal Care (protocol #0221-023-24).

Note that full information on the approval of the study protocol must also be provided in the manuscript.